Enhancing the reaction of municipal solid waste incineration (MSWI) bottom ash in blast furnace slag-based alkali-activated blends

A novel strategy and underlying mechanism

Chen, Boyu; Ye, Guang

DOI
10.1016/j.cemconcomp.2025.106056

Publication date
2025

Document Version
Final published version

Published in
Cement and Concrete Composites

Citation (APA)
Chen, B., & Ye, G. (2025). Enhancing the reaction of municipal solid waste incineration (MSWI) bottom ash in blast furnace slag-based alkali-activated blends: A novel strategy and underlying mechanism. *Cement and Concrete Composites*, *160*, Article 106056. https://doi.org/10.1016/j.cemconcomp.2025.106056

Cement and Concrete Composites 160 (2025) 106056

Contents lists available at ScienceDirect

Cement and Concrete Composites

journal homepage: www.elsevier.com/locate/cemconcomp

Enhancing the reaction of municipal solid waste incineration (MSWI) bottom ash in blast furnace slag-based alkali-activated blends: A novel strategy and underlying mechanism

Boyu Chen [a,*], Guang Ye [a,b]

[a] Department of Materials and Environment (Microlab), Faculty of Civil Engineering and Geoscience, Delft University of Technology, Delft, the Netherlands
[b] Magnel-Vandepitte Laboratory, Department of Structural Engineering and Building Materials, Ghent University, 9052, Ghent, Belgium

ARTICLE INFO

Keywords:
MSWI bottom ash
Pre-activation
Reaction mechanism
Blast furnace slag
Alkali-activated materials

ABSTRACT

Compared with blast furnace slag (BFS), the less reactive MSWI bottom ash (MBA) plays a minor role in alkali-activated blends. This research optimized the use of MBA as a precursor by enhancing its contribution to strength and microstructure development. The proposed strategy combines pre-treatment with pre-activation processes, enabling MBA to react before BFS addition. The NaOH-based pre-treatment led to the oxidation of metallic aluminum and the partial dissolution of the amorphous phase in MBA. The subsequent pre-activation resulted in the generation of C-A-S-H gel, which promoted later-stage gel formation in the paste. The reacted bottom ash particles exhibited distinct features in alkali-activated pastes. Compared with 100 % slag-based system, blending slag with MBA accelerated the slag reaction at late ages and facilitated the formation of a more polymerized C-(N-)A-S-H gel. The compressive strength results indicate that MBA is a promising alternative to Class F coal fly ash in BFS-based alkali-activated blends.

1. Introduction

The increase in global municipal solid waste production has positioned incineration as a preferred waste management strategy, owing to its effectiveness in reducing waste volume, generating energy, and mitigating the environmental impacts of landfill accumulation [1,2]. However, the global expansion of waste-to-energy plants has significantly increased the production of incineration residues, presenting new challenges for their disposal [1,3–10]. The primary residue accounts for approximately 80–90 % of the solid incineration by-products and is known as municipal solid waste incineration (MSWI) bottom ash [3,4]. Given the anticipated scarcity of landfill sites, there is a growing urgency to recycle MSWI bottom ash. One of the most viable options is to use MSWI bottom ash as a raw material for the production of alkali-activated material (AAM) [11,12].

The use of AAM as a construction material is a sustainable option, as it allows for the large-scale recycling of various industrial by-products and reduces the demand for Portland cement [13–21]. A properly designed alkali-activated concrete has a lower carbon footprint and exhibits superior mechanical properties, fire resistance, and long-term durability compared to Portland cement-based concrete [22,23]. However, there is a foreseeable shortage of conventional AAM precursors, especially coal fly ash [24–26]. Using MSWI bottom ash as a substitute for coal fly ash is promising due to its comparable reactivity and global availability [11,27].

MSWI bottom ash requires pre-treatment to improve its quality for use in AAM. The metallic aluminum (Al) found in MSWI bottom ash is detrimental to the strength development of AAM, as it easily oxidizes and leads to hydrogen gas release under high alkaline conditions [28–32]. In previous work, MSWI bottom ash was immersed in NaOH solution to completely oxidize metallic Al prior to its addition to the fresh mixture [30,33–37]. This pre-treatment process is referred to as NaOH solution treatment. The NaOH solution concentration and treatment duration were determined by considering the size of bottom ash particles and the distribution of metallic Al within these particles [11,38].

In most cases, mixing NaOH solution with MSWI bottom ash for pre-treatment was considered a procedure similar to adding part of the activator in advance. The NaOH solution used for pre-treatment was taken from the total amount designed for the activator. The remaining activator was added later while mixing fresh paste [12]. Previous research mainly examined the effectiveness of NaOH solution treatment

* Corresponding author.
E-mail address: B.Chen-4@tudelft.nl (B. Chen).

https://doi.org/10.1016/j.cemconcomp.2025.106056
Received 5 January 2025; Received in revised form 6 March 2025; Accepted 18 March 2025
Available online 20 March 2025

in reducing metallic Al content [30,33–37]. The reactivity change induced by NaOH solution treatment was also studied [39]. However, there is no information on the extent to which MSWI bottom ash reacts during NaOH solution treatment or how the resulting reaction products affect the microstructure development of AAM.

MSWI bottom ash as the sole precursor for AAM preparation is not recommended due to the low compressive strength and high heavy metal leaching risks of resulting binder products [12]. When preparing AAM using 100 % MSWI bottom ash, the fresh mixture requires more than one day to harden under ambient temperature [27,28,40,41]. The performance of MSWI bottom ash-based AAM is often improved by incorporating blast furnace slag [12]. Previous researchers investigated the properties of AAM made from a blend of blast furnace slag and MSWI bottom ash, with a focus on compressive strength [12]. The strength was found to be influenced by several factors, such as the metallic Al content, reactivity, and dosage of MSWI bottom ash, the composition of the activator, and the curing conditions [30,33,34,36,37].

In the binary AAM system, blast furnace slag, being more reactive than MSWI bottom ash, plays a more significant role in strength development [11,27]. It is not well understood how MSWI bottom ash contributes to reaction product formation and subsequently influences the strength and microstructure development of alkali-activated blast furnace slag/MSWI bottom ash [12]. Current methods to enhance the contribution of MSWI bottom ash focus on improving its reactivity [12]. These quality-upgrade treatments are energy-intensive, typically involving thermal treatment to form reactive mineral phases or mechanical treatments to reduce particle size [11]. Despite this, no research has explored low-energy approaches to promoting the reaction of MSWI bottom ash when it is used in combination with more reactive precursors.

As discussed above, significant engineering advancements have been made in using MSWI bottom ash to prepare AAM. However, the limited understanding of how MSWI bottom ash contributes to microstructure formation hinders the development of energy-efficient strategies to promote its contribution. To address this, the present research not only aims to enhance the role of MSWI bottom ash in alkali-activated blast furnace slag/MSWI bottom ash pastes but also provides a detailed investigation into the mechanisms driving this enhancement. This knowledge enables the effective utilization of MSWI bottom ash as an AAM precursor. The present study is divided into two main sections, as shown in Fig. 1 and outlined below:

- A novel sample preparation strategy is proposed to enhance the role of MSWI bottom ash in alkali-activated blast furnace slag/MSWI bottom ash pastes. This approach involves sequential pre-treatment and pre-activation processes. The reactions that occurred during these two processes were investigated, and their combined effects on strength development and microstructure formation of AAM were explored.
- The microstructure of AAM is analyzed in terms of reaction kinetics, reaction degree, reaction products, and pore volume to understand the contribution of MSWI bottom ash. The alkali-activated blast furnace slag/MSWI bottom ash pastes prepared using the highest dosage of MSWI bottom ash are used for microstructure analysis. The

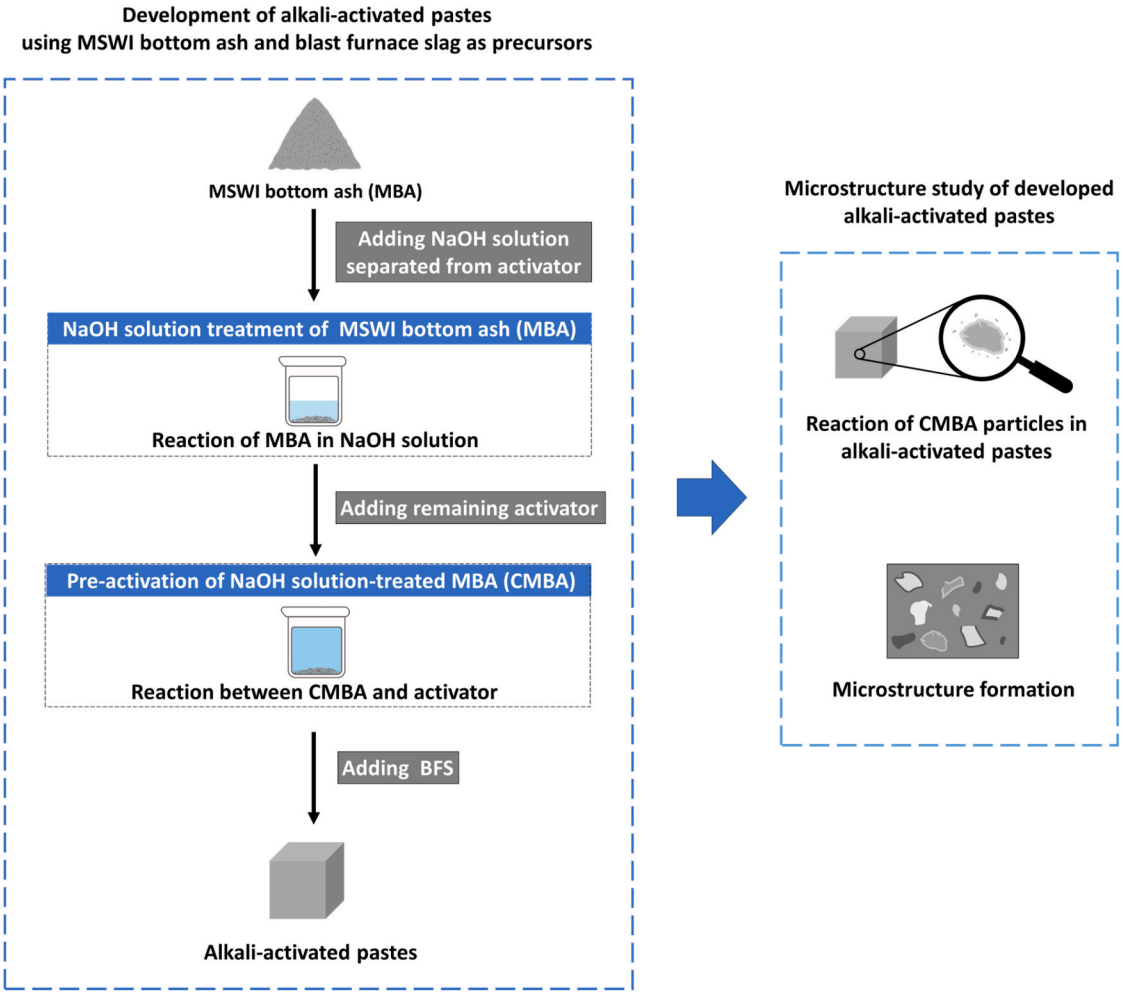

Fig. 1. The outline of this research.

reference samples include alkali-activated blast furnace slag pastes, alkali-activated blast furnace slag/Class F coal fly ash pastes, and alkali-activated blast furnace slag/micronized sand pastes.

2. Materials and methods

2.1. Materials

The precursors used for AAM sample preparation include MSWI bottom ash (MBA), blast furnace slag (BFS), Class F coal fly ash (FA), and micronized sand (M300). Detailed information on the particle size, chemical and mineralogical compositions, and reactivity of MBA, BFS, and FA is presented in our previous study [27]. For the particle size and compositional details of M300, please also refer to our previous publication [42]. The MBA used in this work exhibits typical chemical and mineralogical characteristics of MSWI bottom ash [11,27]. FA and M300 were selected as reference materials for MBA. This selection was based on the comparable reactivity between FA and MBA as AAM precursors [27]. The M300 is a non-reactive quartz powder, and its particle size is similar to that of MBA [42]. The NaOH pellets (analytical grade, purity ≥98 %), water glass solution (8 wt% Na_2O and 26.9 wt% SiO_2), and deionized water were used to prepare the activator.

2.2. Mix design

As indicated in our previous research [27], combining MBA with BFS for AAM preparation could mitigate the risk of excessive heavy metal leaching from MBA-based AAM and improve its compressive strength. The percentage of MBA in the precursor of AAM was recommended to be lower than 50 wt%. Therefore, in this work, the replacement levels of MBA for BFS were selected to be 10 wt%, 20 wt%, and 30 wt%. The maximum dosage of MBA is set at 30 wt% because if this level is exceeded, the amount of solution required for the NaOH solution treatment of MBA will surpass what is available from the activator.

The Na_2O content in the activator, calculated as the ratio of the Na_2O mass in the activator to the precursor mass, was set at 5 wt%. This is because when the Na_2O content exceeds 5 wt%, some of the Si released from MBA is expected to remain in the pore solution rather than participating in the formation of stable reaction products [27]. Moreover, since MBA and Class F coal fly ash exhibit similar reactivity, the Na_2O content optimized for the blast furnace slag-Class F coal fly ash binary AAM system should be applicable to the blast furnace slag-MSWI bottom ash system [27]. High compressive strength can be achieved for AAM made from a blend of blast furnace slag and Class F coal fly ash when the activator contains around 5 wt% Na_2O [43].

The molar ratio between SiO_2 and Na_2O in the activator, also referred to as the alkali modulus (Ms), is chosen to be one. This value is determined with reference to the optimal range of Ms (between 1 and 1.5) for alkali-activated blast furnace slag/coal fly ash [44]. Huang et al. [33,37] also reported that the optimal Ms was 1.04 when using MSWI bottom ash and blast furnace slag to prepare AAM.

In addition to the MBA-containing mixture, other types of paste samples were also made for comparison. Based on the precursor used, all the alkali-activated pastes investigated in this work are classified into five distinct categories: 100 BFS AAM, FA-BFS AAM, M300-BFS AAM, MBA-BFS AAM, and CMBA-BFS AAM. The mix design of these paste samples can be found in Table 1.

The 100 BFS AAM is the alkali-activated paste prepared using only BFS as the precursor. The FA-BFS AAM, M300-BFS AAM, MBA-BFS AAM, and CMBA-BFS AAM are alkali-activated pastes made from BFS and another type of precursor. The raw materials used to prepare MBA-BFS AAM and CMBA-BFS AAM are the same, but the sample preparation procedures are different (see section 2.3).

Table 1
Mix design of alkali-activated paste samples.

Sample names	Precursors (wt.%)				Activator
	FA	MBA	M300	BFS	
100 BFS AAM	–	–	–	100	• Water-to-precursor mass ratio: 0.35 • Na_2O content: 5 wt% • Alkali modulus: 1
10 FA-BFS AAM	10	–	–	90	
10 MBA-BFS AAM	–	10	–		
10 CMBA-BFS AAM[a]	–	10	–		
20 FA-BFS AAM	20	–	–	80	
20 CMBA-BFS AAM[a]	–	20	–		
30 FA-BFS AAM	30	–	–	70	
30 CMBA-BFS AAM[a]	–	30	–		
30 M300-BFS AAM	–	–	30		

[a] The sample preparation procedure included both the NaOH solution treatment and pre-activation process.

2.3. Samples preparation

Fig. 2 (a) depicts the sample preparation procedure for CMBA-BFS AAM. The precursors are MBA and BFS. The activator was prepared in two parts. One part is a NaOH solution (3 mol/L) made by dissolving NaOH pellets in deionized water. The other part, also referred to as the remaining activator, is a mixture of water glass solution, NaOH pellets, and distilled water.

While preparing CMBA-BFS AAM, MBA was first mixed with NaOH solution (3 mol/L) to oxidize metallic Al. The mass ratio between the NaOH solution and MBA is 0.7. The mixture of MBA and NaOH solution is called “slurry” in this paper. The freshly mixed slurry was transferred to a polyethylene bottle for room-temperature storage (see Fig. 3). The bottle was tightly closed to prevent water evaporation. The amount of metallic Al that remained in the slurry was monitored over time using the water displacement method [38]. For details on measuring metallic Al in slurry, please refer to our previous work [42]. The duration of NaOH solution treatment was determined at the point when the metallic Al content reached zero.

It took five days for the NaOH solution treatment to dissolve all the metallic Al in the MBA. This is because some metallic Al present in MBA is covered by mineral phases, which act as protective layers, inhibiting further dissolution [38]. Although the proposed NaOH solution treatment method is somewhat time-consuming, it is designed to demonstrate an extremely low-energy consumption scenario by avoiding the need to raise temperature. It is also common in previous research to perform NaOH solution treatment at room temperature [12]. The undissolved bottom ash particles in the 5-day slurry are referred to as *NaOH solution-treated MBA* (CMBA) in this text (see Fig. 3).

After NaOH solution treatment, the remaining activator was added to the 5-day slurry. The mixture of slurry and activator was cured at room temperature for 24 h. During this process, the CMBA in the slurry was pre-activated. After the pre-activation process, the 1-day mixture was blended with BFS using an IKA® T 50 ULTRA-TURRAX® high-shear mixer to prepare the fresh pastes of CMBA-BFS AAM. The same mixer was also used to prepare other types of paste samples.

While the raw materials are identical, the preparation method for MBA-BFS AAM is not the same as that of CMBA-BFS AAM. As depicted in Fig. 2 (b), the activator was directly added to the dry mixture of BFS and MBA. After 4 min of mixing, the fresh pastes of MBA-BFS AAM were prepared. The same sample preparation method was applied to the FA-BFS AAM, M300-BFS AAM, and 100 BFS AAM.

The fresh pastes were cast into cubic molds with a side length of 20 mm. The paste samples were initially cured in molds for 1 day at room temperature. After being removed from the molds, the specimens were wrapped in plastic film and placed in a curing room at 20 °C and 99 % relative humidity until the specified test age.

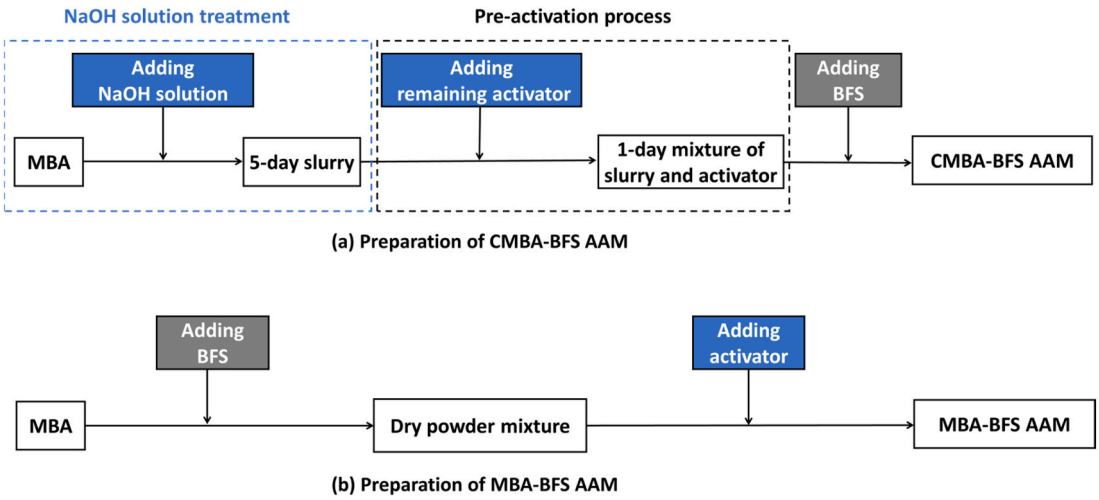

Fig. 2. Sample preparation procedures for (a) CMBA-BFS AAM and (b) MBA-BFS AAM. The sample preparation procedure for FA-BFS AAM and M300-BFS AAM is the same as that for MBA-BFS AAM.

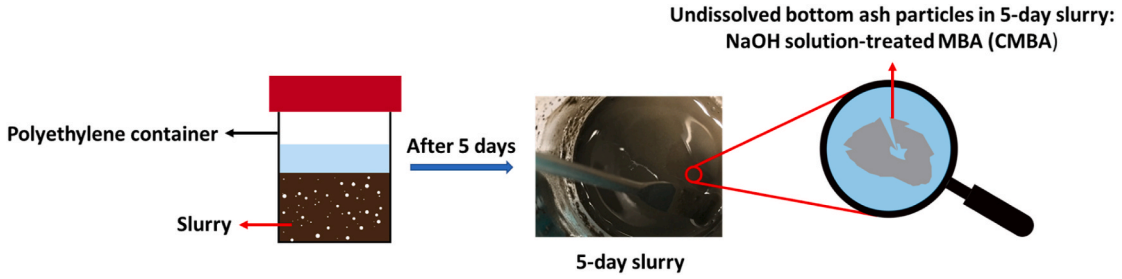

Fig. 3. Illustration of the NaOH solution treatment of MBA.

2.4. Studies of reactions occurred during sample preparation process

2.4.1. Reaction of MBA during pre-treatment process

The heat generated during NaOH solution treatment of MBA was recorded using a TAM-AIR-314 isothermal conduction calorimeter. The calorimetry test was conducted following the guidelines outlined in [45], with the temperature in the calorimeter maintained at 20 °C. Around 10 g of slurry was sealed in a glass ampoule and loaded into the calorimeter. The slurry was prepared by mixing MBA with NaOH solution.

2.4.2. Characterization of CMBA-Residue obtained from pre-treatment process

The CMBA-Residue refers to the solid material obtained after drying the 5-day slurry for over three months at −24 °C and 0.1 Pa in a vacuum freeze-dryer. The slurry, resulting from NaOH solution treatment, was neither washed nor filtered before drying. Fig. 4 demonstrates the preparation process of CMBA-Residue. This approach ensured that the CMBA, residual NaOH solution, and potential reaction products formed during the treatment were fully retained in the CMBA-Residue.

The CMBA-Residue was analyzed using X-ray diffraction (XRD) and quantitative X-ray diffraction (QXRD) to identify the newly formed phases and quantify their contents. The XRD measurements and QXRD analysis were performed following the methods described in our

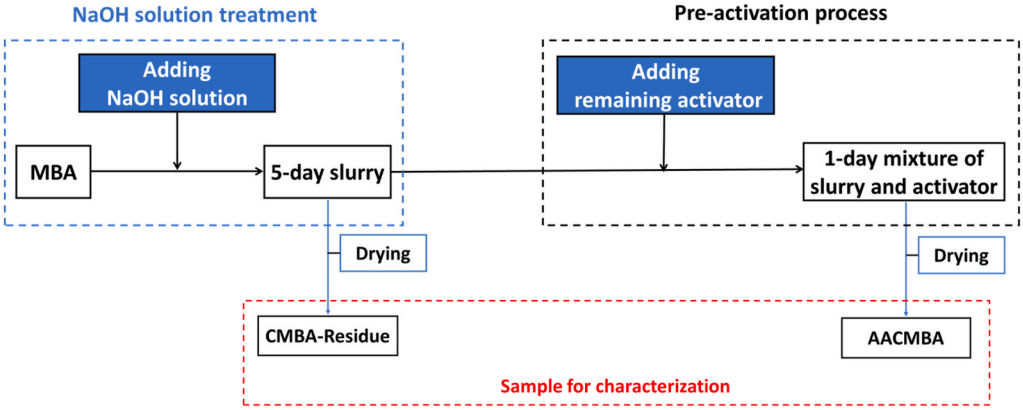

Fig. 4. The preparation process of CMBA-Residue and AACMBA for characterization.

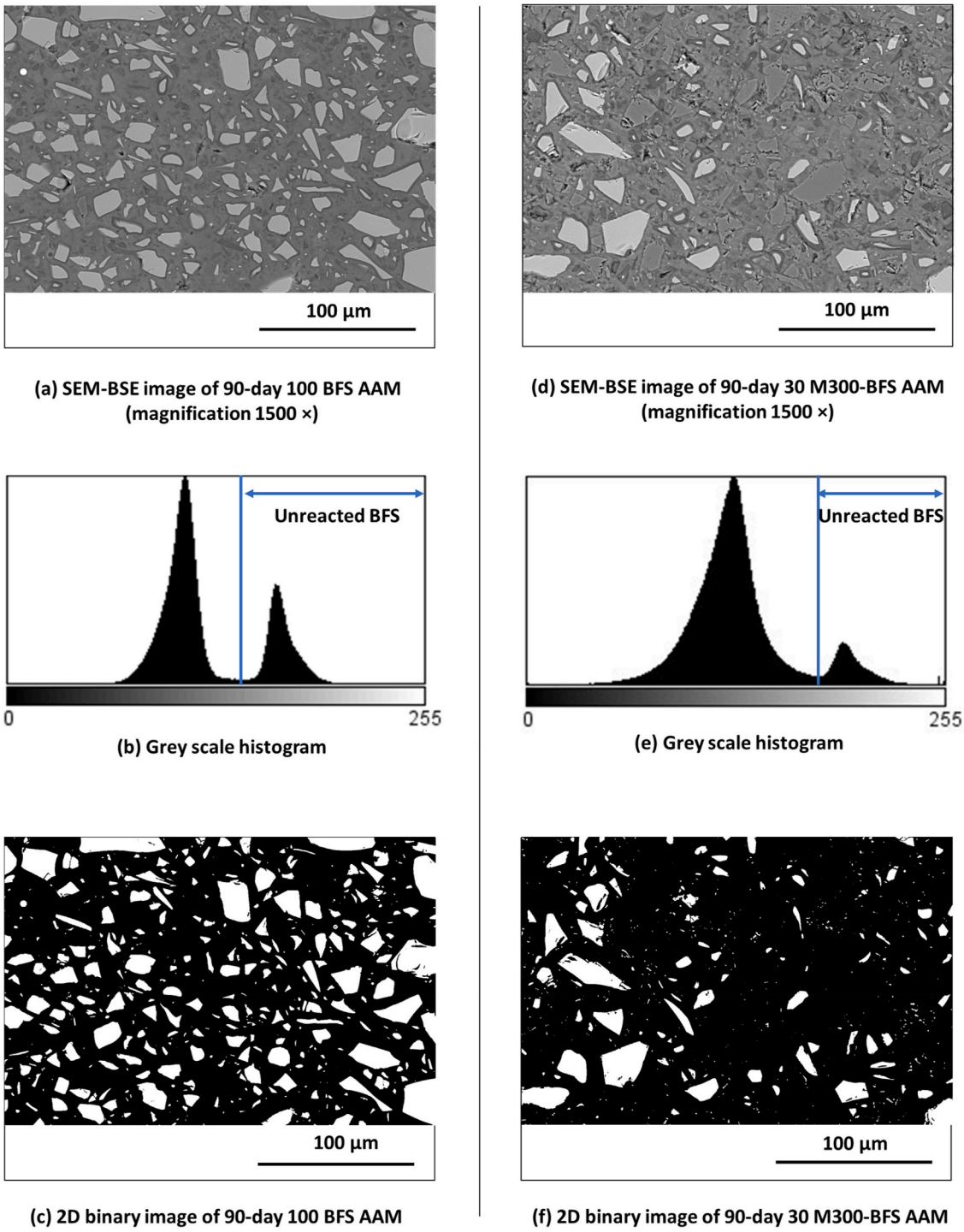

Fig. 5. Phase segmentation of 90-day 100 BFS AAM and 90-day 30 M300-BFS AAM. The white particles in the two-dimensional (2D) binary images are segmented unreacted BFS particles.

previous work [27,42]. The accuracy of QXRD analysis is typically limited to around 0.5 wt% [46]. In this study, QXRD data for MBA were not collected, as they had already been reported in our previous publication [27].

The chemical bonds within CMBA-Residue were analyzed with Attenuated Total Reflectance-Fourier Transform Infrared (ATR-FTIR) spectroscopy. The model of the instrument is PerkinElmer Spectrum 100. The FTIR spectra were recorded across the wavenumber range of 4000-600 cm^{-1} at a resolution of 1 cm^{-1}. The FTIR data from MBA and the glass particles within it were recorded for comparison. More detailed information about the separation of glass particles can be found in our previous work [27]. The FTIR measurements for all samples were conducted under identical conditions.

2.4.3. *Reaction of CMBA during pre-activation process*

The reaction of CMBA during the pre-activation process was studied by monitoring the heat evolution using a TAM-AIR-314 isothermal conduction calorimeter. The test procedure, sample mass, and test conditions are the same as those described in section 2.4.1. The only difference is that the test sample was prepared by mixing the 5-day

slurry obtained after NaOH solution treatment with the remaining part of the activator. The CMBA particles are present in the 5-day slurry.

2.4.4. Characterization of AACMBA obtained from pre-activation process

The AACMBA (alkali-activated CMBA) refers to the solid obtained after drying the 1-day mixture produced after the pre-activation process (see Fig. 4). The drying process for the 1-day mixture was identical to that used for the 5-day slurry (see Section 2.4.2). Similarly, no washing or filtering was performed before drying. In this case, the unreacted CMBA, residual activator, and potential reaction products formed after the pre-activation process can all be detected during characterization. The characterization techniques (including QXRD and FTIR) used for CMBA-Residue were also applied to analyze the mineral phases and chemical bonds in AACMBA. The tests were performed under the same conditions as those for CMBA-Residue.

2.5. Paste sample characterization

The alkali-activated paste samples were characterized from the following perspectives: compressive strength, reaction kinetics, inner structure, pore characteristics, reaction products, and reaction degree. The dried samples used for characterization were prepared by stopping the alkali-activation reaction with the isopropanol exchange method, followed by drying in a vacuum desiccator [45]. Although the solvent-exchange method was originally developed to stop cement hydration, it has been proved to be the most suitable method for stopping the reaction in AAM [47]. Grinding was performed in a nitrogen glove box to prepare powder samples for characterization.

2.5.1. Compressive strength and reaction kinetics

The compressive strength tests were performed on 1-, 7-, 28-, and 90-day samples in accordance with the NEN-EN 196–1:2016 standard [48]. The reaction kinetics of AAM were measured using TAM-AIR-314 isothermal conduction calorimeter. The calorimetric tests were conducted following the ASTM C1697 standard [49].

2.5.2. Inner structure

The inner structure of 1-day CMBA-BFS AAM was visualized using micro-computed tomography (Micro-CT), a technique that enables non-destructive 3D imaging of the specimen. The goal is to confirm the absence of cracks in the sample, thereby ensuring that the NaOH solution treatment is effective in preventing metallic Al-induced cracking and volume expansion. The test samples were wrapped with cling film to prevent moisture loss during the scanning process. More details on the settings of the Micro-CT scanner and the processing of CT scan data can be found in our previous publication [42].

2.5.3. Pore characteristics and reaction products

The pore volume and pore size distribution in hardened alkali-activated pastes was determined using a nitrogen adsorption test (Gemini VII 2390). This test is suitable for characterizing the pores in AAM, as the abundance of nano pores is a key feature of AAM [50,51]. For the measurement, the relative pressure (P/P_0) ranged from 0.05 to 0.99. The volume and diameter of pores were calculated based on the Barret-Joyner-Halenda model [52].

The crystalline reaction products formed in AAM were identified with XRD. The crystalline and amorphous phase contents in AAM were determined using QXRD analysis. The chemical bonds within the gel formed in AAM were characterized by ATR-FTIR.

The backscattered electron (BSE) images were acquired using the FEI QUANTA FEG 650 ESEM to analyze the compositional contrast and morphology of the hardened alkali-activated pastes. The scanning electron microscopy (SEM) operated at an electron beam voltage of 15 kV with a working distance set to 10 mm. The elemental composition of the gel phases was determined using the Energy Dispersive X-ray spectroscopy (EDS) detector integrated within the SEM. Around 200 distinct points within the regions containing reaction products were selected for EDS spot analysis. The test samples were prepared by first mounting them in epoxy resin, followed by grinding and polishing with ethanol (≥96 % v/v, TechniSolv®). A thin carbon coating (approximately 10 nm thick) was applied under high vacuum conditions to enhance the conductivity of the polished samples.

2.5.4. Reaction degree of BFS in AAM

The reaction degree of the BFS in AAM was determined to study the effects of CMBA or M300 on the reaction of BFS. The reaction degree of BFS in hardened alkali-activated pastes can be calculated with the equation: $\alpha(t) = (1 - \frac{V_t}{V_0}) \times 100\ \%$, where $\alpha(t)$ is the degree of reaction at age t, V_t is the volume fraction of BFS at age t, and V_0 is the initial volume fraction of BFS in the pastes [53–55]. The volume fraction of unreacted BFS in hardened pastes was determined by calculating the area fraction of unreacted BFS in SEM-BSE images using the image analysis method. More details about this method can be found in the Appendix. The area fraction of BFS in hardened pastes was calculated for the SEM-BSE images of 100 BFS AAM, 30 M300-BFS AAM, and 30 CMBA-BFS AAM paste samples. Examples of the phase segmentation process are shown in Figs. 5 and 7.

The thresholding method proposed by Prewitt et al. [56] was used to segment the unreacted BFS particles in the SEM-BSE images of 90-day 100 BFS AAM and 90-day 30 M300-BFS AAM. This approach was

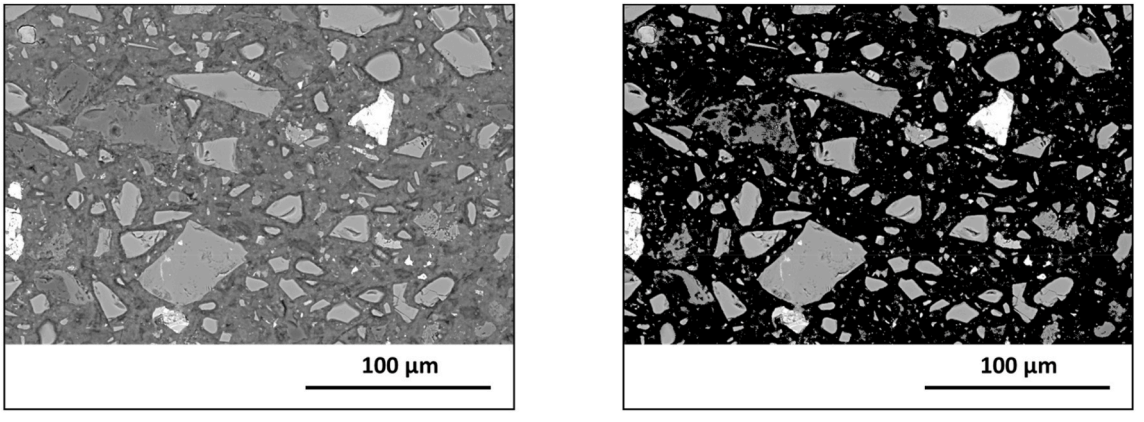

Fig. 6. (a) SEM-BSE image of 90-day 30 CMBA-BFS AAM and (b) output image obtained after Trainable Weka Segmentation analysis.

chosen because the grey scale histogram of the SEM-BSE image (see Fig. 5 (a) and (d)) exhibits a bimodal distribution with two distinct peaks (Fig. 5 (b) and (e)). The threshold was determined as the minimum point between the two peaks in the histogram. After the thresholding operation, pixels representing the unreacted BFS particles were separated. In obtained two-dimensional (2D) binary images (Fig. 5 (c) and (f)), the white area corresponds to the unreacted BFS particles. The phase segmentation was performed with the image processing program ImageJ.

The unreacted BFS particles in the SEM-BSE images of 90-day 30 CMBA-BFS AAM were identified through a different method. First, all particles in the SEM-BSE images were segmented based on their grey levels. Then, the EDS mappings were used to identify which segmented particles are BFS. This method was used because, although the grayscale of BFS particles in the SEM-BSE image of 90-day 30 CMBA-BFS AAM is very different from that of the gel matrix, some CMBA particles have brightness comparable to BFS particles and the gel matrix due to their compositional similarity (see Fig. 6 (a)).

The pixels of the SEM-BSE image of 30 CMBA-BFS AAM (Fig. 6 (a)) were separated into "gel phases" and "particles" using the Trainable Weka Segmentation plugin in ImageJ. This Fiji plugin integrates various machine learning algorithms with chosen image features to generate pixel-based segmentations. The "particles" separated include unreacted CMBA particles, unreacted BFS particles, and reaction products that are brighter than the surrounding gel matrix. The reference pixels corresponding to the "gel phases" and "particles" were manually selected to train the classifier, then the remaining pixels of the SEM-BSE images can be segmented automatically. The output image of Trainable Weka Segmentation is illustrated in (Fig. 6 (b)).

The unreacted BFS particles were identified by combining the SEM-BSE image with the EDS elemental mappings of Mg, Ca, Al, and Si. An example of these elemental mappings is presented in Appendix Figure 2. The acquisition time for each complete set of elemental maps is 1745 s.

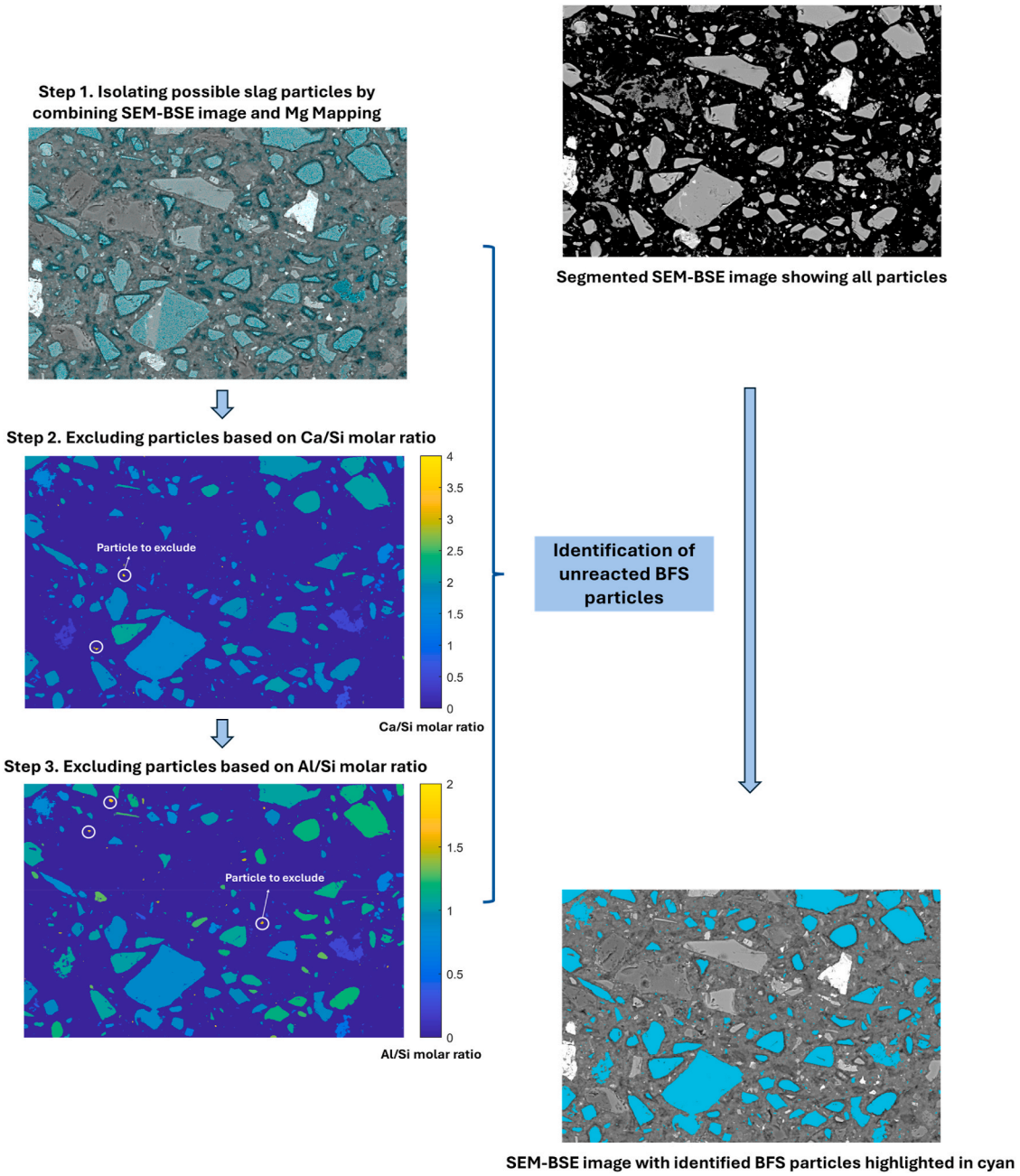

Fig. 7. Proposed procedure for identifying BFS particles in 90-day 30 CMBA-BFS AAM.

The dwell time is 50 μs. Fifteen mapping data sets were obtained for image analysis to determine the average area fraction of unreacted BFS particles in 90-day 30 CMBA-BFS AAM. The proposed phase identification procedure consists of three steps, which are detailed below and illustrated in Fig. 7. After all these three steps, the identified BFS particles were colored cyan on the SEM-BSE image.

- Step 1 Identify particles that have a grey level corresponding to BFS and also contain Mg. The SEM-BSE image (Fig. 6 (a)) and EDS elemental mapping of Mg (Appendix Figure 2 (a)) were used for the analysis. This method was previously used by Kocaba et al. [57] to identify blast furnace slag in blended cement pastes.
- Step 2 Calculate the Ca/Si molar ratio based on the elemental mapping dataset of Ca and Si for particles selected in step 1 and exclude the particles that exceed the range of this ratio in BFS particles (0.05–3.16). The EDS elemental mappings of Ca and Si are shown in Appendix Figure 2 (b) and (d), respectively. The reference range for the Ca/Si molar ratio was obtained by analyzing the unreacted BFS particles in 100 BFS AAM samples. The histogram in Appendix Figure 3 (a) presents the distribution of the Ca/Si molar ratio for over 17000 unreacted BFS particles.
- Step 3 Calculate the Al/Si molar ratio based on the elemental mapping dataset of Al and Si for particles selected in step 2 and exclude the particles that exceed the range of this ratio in BFS particles (0.02–1.23). The EDS elemental mappings of Al and Si are presented in Appendix Figure 2(c) and (d), respectively. The reference range for the Al/Si molar ratio was determined using the same method as for the Ca/Si ratio. The distribution of the Al/Si ratio was demonstrated in Appendix Figure 3 (b).

3. Results and discussion

3.1. Reactions occurred during NaOH solution treatment and pre-activation process

In this section, the reactions that occurred during the NaOH solution treatment of MBA and the pre-activation of CMBA are discussed, with a focus on the combined effects of these two processes on reaction product formation.

3.1.1. Heat release during pre-treatment process

The heat release during the NaOH solution treatment of MBA is recorded in the curves presented in Fig. 8. In the heat flow curve, the first peak with an intensity of 18 mW/g corresponds to the wetting and dissolution of MBA (see Fig. 8 (b)). The dissolution of MBA mainly concerns the oxidation of metallic Al, which proceeds rapidly under alkaline conditions. While the complete oxidation of metallic Al takes 5 days, most of the metallic Al reacts within the first day. After this initial phase, the remaining Al oxidizes at a slower rate, releasing heat that is insufficient to produce a detectable peak [42]. The second peak appeared at 1.5 days with an intensity of 0.04 mW/g (see Fig. 8 (c). Despite the minimal intensity of this peak, its appearance suggests the formation of gel phases. After 2 days, continuous heat release was recorded, suggesting ongoing dissolution of MBA (see Fig. 8 (d)).

3.1.2. Chemical changes induced by pre-treatment process

The analysis of CMBA-Residue provides insights into the presence of unconsumed NaOH, formation of reaction products, and compositional changes of MBA after NaOH solution treatment. As presented in Fig. 9, the XRD patterns of MBA and CMBA-Residue are nearly identical, with a

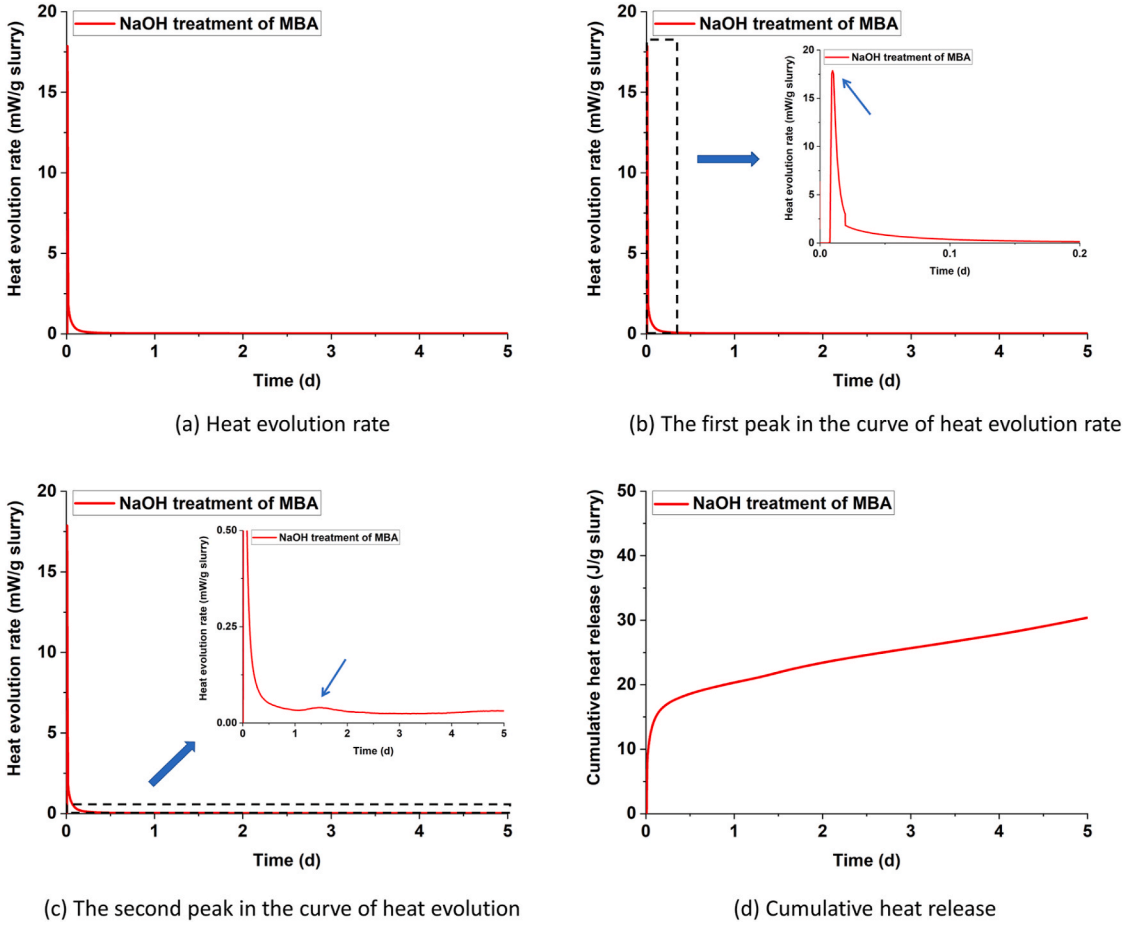

Fig. 8. (a)–(c) Heat evolution rate and (b) cumulative heat release per gram of slurry. The slurry is prepared for the NaOH solution treatment of MBA.

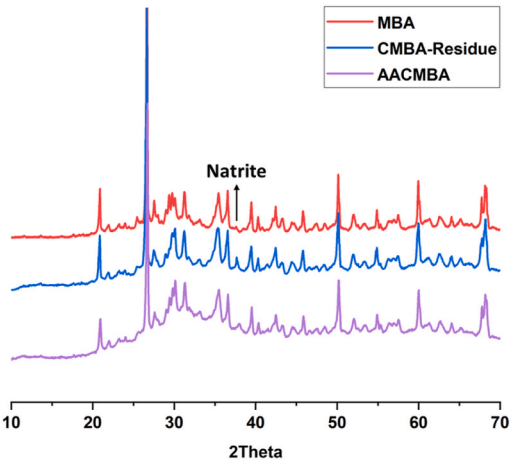

Fig. 9. XRD patterns of MBA, CMBA-Residue, and AAMBA.

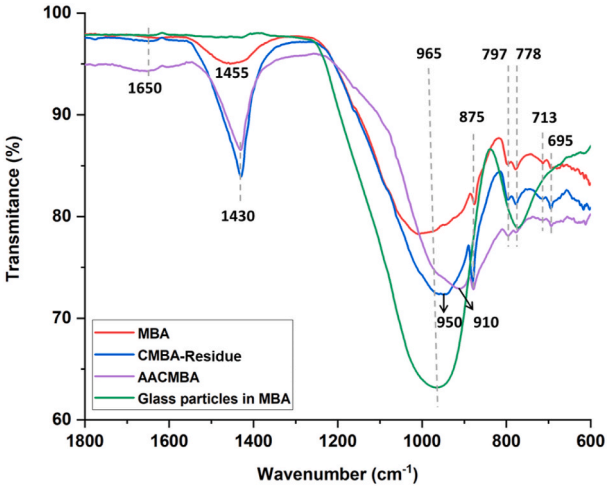

Fig. 10. FTIR spectra of MBA, CMBA-Residue, AAMBA, and glass particles in MBA.

notable difference at 2θ of 37.7°. This peak is assigned to natrite (Na_2CO_3), which appears only in the XRD pattern of CMBA-Residue. This carbonate phase was detected due to the carbonation of the unconsumed NaOH. The FTIR spectra shown in Fig. 10 also reveal differences associated with the presence of natrite. The carbonate bands at 1430 cm^{-1} and 875 cm^{-1} in the CMBA-Residue spectrum exhibit higher intensity compared to those in the MBA spectrum. The detailed band assignments in the FTIR spectra of MBA and CMBA-Residue are listed in Table 2.

The broad band centered at 950 cm^{-1} in the FTIR spectrum of CMBA-Residue corresponds to the stretching vibration of the Si-O-T bonds (T: tetrahedral Si or Al). The vibration of the Si-O-T bonds in calcium aluminosilicate hydrate (C-A-S-H) gel occurs at the same wavenumber [58–60]. A band at 1650 cm^{-1}, albeit with low intensity, was detected in the FTIR measurement of CMBA-Residue. This band is usually attributed to the bending vibration of the H-OH bond, which is the typical resonance of water within the gel phases [60]. The detection of the Si-O-T bond and the H-OH bond indicates the presence of a trace amount of C-A-S-H gel in CMBA-Residue. This gel phase formation was also evidenced by the emergence of a second peak in the calorimetric analysis (see Fig. 8 (c)). Additionally, previous researchers also identified C-A-S-H gel as a reaction product of MSWI bottom ash and alkaline solution [12].

Table 2
Band assignments for FTIR spectra of MBA, CMBA-Residue, and AACMBA shown in Fig. 10.

Wavenumber (cm^{-1})	Assignment	Description
1650	Bending vibration of H-OH bond [60]	Bonds in the water within gel phases
1455, 1430	Stretching vibration of C-O [64,65]	Bonds in carbonates
875, 713	Bending vibration C-O [64]	
797, 778, 695	Vibrations of Si-O [64]	Characteristic bonds in quartz

The noticeable change in the main band of CMBA-Residue compared to MBA can be explained by the combined effects of the amorphous phase dissolution and the C-A-S-H gel formation during NaOH solution treatment. The main band observed in MBA can be attributed to the stretching vibration of the Si-O-Si bond of the glass network [61]. This band is broad and centered at 965 cm^{-1}, the same wavenumber as the main band observed in the FTIR spectrum of the glass particles in MBA (see Fig. 10). In comparison to MBA, the main band of CMBA-Residue is sharper, and its center is positioned at a lower wavenumber (950 cm^{-1}). This sharper band indicates increased structural order in the bonds, which is partially caused by the dissolution of the amorphous phase in MBA. The silicon released by MBA during NaOH solution treatment is likely to present in monomeric form, similar to the silicate monomers found after the dissolution of waste glass in NaOH solution [62]. The silicate monomers can react with the $Al(OH)_4^-$ species dissolved by MBA and form Si-O-Al complexes and C-A-S-H gel [63], contributing to the observed shift of the main band to 950 cm^{-1}.

3.1.3. Heat release during pre-activation process

The reaction of CMBA during pre-activation process was studied by measuring the reaction heat. In the heat evolution curve (Fig. 11 (a)), the calorimetric peak associated with wetting and dissolution is negligible. The reason is that no additional solid was added to the mixture. The main peak appeared at around 0.12 days. The appearance of this exothermic peak is due to the gel phase formation. The intensity of the main peak observed during the 1-day pre-activation of CMBA (Fig. 11 (a)) is much higher than the second calorimetric peak detected during the NaOH solution treatment of MBA (Fig. 8 (c)). This peak intensity difference suggests that more gel phases are formed after the pre-activation of CMBA.

3.1.4. Reaction products formed after pre-activation process

The reaction products formed after the pre-activation process can be identified by characterizing AACMBA. The XRD and FTIR results both indicate the formation of more gel phases after the pre-activation process. The hump corresponding to the amorphous phase is more pronounced in the XRD pattern of AACMBA than in those of MBA and CMBA-Residue (see Fig. 9). According to the QXRD analysis, the amorphous phase content in AACMBA is slightly higher than in MBA and CMBA-Residue (Table 3). In the FTIR spectra of AACMBA and CMBA-Residue (Fig. 10), the band at 1650 cm^{-1} is assigned to the H-OH bond within the gel phases [60]. This band is more pronounced in the AACMBA spectrum than in the spectrum of CMBA-Residue. Table 2 provides the detailed band assignments in the FTIR spectrum of AACMBA.

The main band in the spectrum of AACMBA appears at a lower wavenumber (910 cm^{-1}) and is narrower than that in CMBA-Residue (Fig. 10). This shift to a lower wavenumber indicates that some Si^{4+} ions in the Si-O-T bond have been substituted by Al^{3+} ions, as the bonding force of Al-O is weaker than that of the Si-O bond [58,66]. Moreover, the incorporation of Na^+ into the Si-O-T network also causes a significant shift of the band associated with its asymmetric stretching vibration to lower wavenumbers [67]. The molecular vibrational constant of the Si-O-Na bond was lower compared to the Si-O-T bond. From the preceding analysis, it can be inferred that more gel phases are

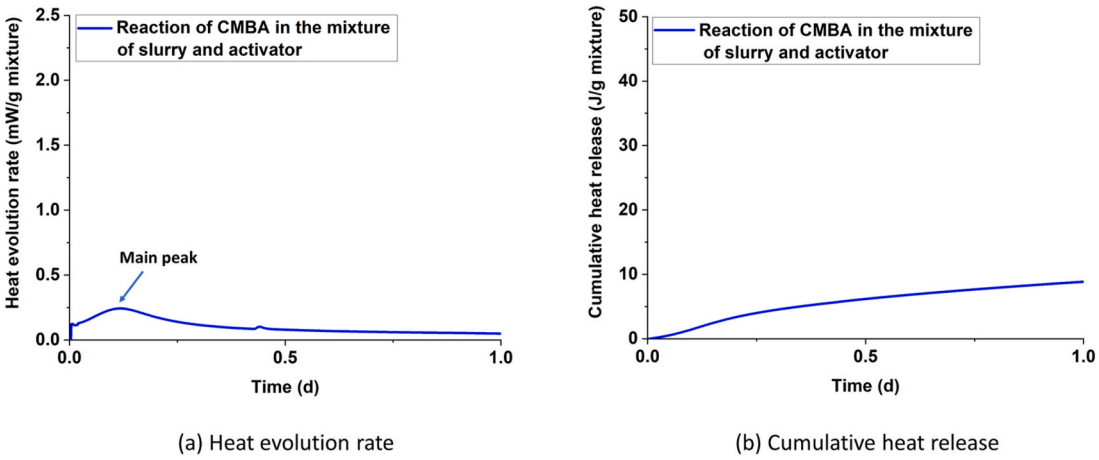

Fig. 11. (a) Heat evolution rate and (b) cumulative heat release per gram of the mixture of 5-day slurry and activator. The 5-day slurry is obtained after the NaOH solution treatment of MBA and thus contains CMBA.

present in AACMBA than in CMBA-Residue.

The pre-activation process can lead to the formation of C-A-S-H gel and albite. The C-A-S-H gel had already formed after the NaOH solution treatment of MBA. The pre-activation process further promoted the formation of this gel, resulting in a higher C-A-S-H gel content in AACMBA. Albite was reported to be a crystalline reaction product formed after the alkali activation of MSWI bottom ash [12,30,68]. The addition of NaOH solution and activator to MBA increased the total mass. As a result, the relative content of the minerals initially present in MBA should be lower in CMBA-Residue and AACMBA. However, the albite content increased continuously after the NaOH solution treatment of MBA and the pre-activation of CMBA (Table 3). The difference in albite content between CMBA-Residue and AACMBA exceeds the accuracy limit of QXRD analysis (0.5 wt% [46]), confirming that the observed increase in albite content is reliable. Therefore, albite is formed as a reaction product during the pre-activation process. Furthermore, the formation of albite suggests the presence of sodium aluminosilicate hydrate (N-A-S-H) gel, which can form under the same condition [69].

3.2. *Impact of proposed sample preparation strategy on volume expansion and compressive strength*

When MBA was directly mixed with BFS to prepare AAM, volume expansion was observed even at the ash dosage of 10 wt%. As shown in Fig. 12, the height of the 10 MBA-BFS AAM specimen is higher than that of the mold (2 cm). This expansion occurs because MBA was not treated to reduce its metallic Al content to zero. The risks of cracking and volume expansion were eliminated for samples prepared using the proposed strategy. The 2D binary images and three-dimensional (3D) images obtained from the CT scan indicate that only pores are present within CMBA-BFS AAM (see Fig. 13). Since metallic Al has been fully oxidized during NaOH solution treatment, these pores are mainly air bubbles entrained in the fresh pastes during the sample preparation process.

By applying the proposed sample preparation strategy, MBA can successfully replace FA in alkali-activated FA-BFS pastes without compromising compressive strength. Fig. 14 (a) shows that the 28-day compressive strength of CMBA-BFS AAM exceeds that of FA-BFS AAM by 11 % and 21 % at ash dosages of 20 wt% and 30 wt%, respectively. After 90 days (Fig. 14 (b)), the compressive strength of FA-BFS AAM is almost equal to that of CMBA-BFS AAM at the same ash dosage (from 10 to 30 wt%). This similarity in 90-day compressive strength can be

Table 3
XRD and QXRD analysis results of MBA, CMBA-Residue, and AACMBA.

Phases	MBA[a] (wt.%)	CMBA-Residue (wt.%)	AACMBA (wt.%)	Formulae	ICSD codes
Quartz	12.1	11.7	10.7	SiO_2	541929
Cristobalite	0.4	0.3	0.3	SiO_2	1251919
Magnetite	0.9	0.9	0.6	Fe_3O_4	92356
Hematite	0.4	0.3	0.3	Fe_2O_3	453828
Wustite	0.2	0.2	0.0	FeO	309924
Gehlenite	2.8	2.0	0.9	$Ca_2Al_2SiO_7$	1411155
Albite	1.9	2.0	3.1	$NaAlSi_3O_8$	1402109
Orthopyroxene	1.4	1.8	0.9	$Ca_{0.02}Mg_{0.30}Fe_{0.68}SiO_3$	1615622
Diopside	4.4	4.3	3.7	$CaMg_{0.69}Fe_{0.31}Si_2O_6$	77809
Wollastonite	2.6	3.0	3.5	$CaSiO_3$	1253098
Calcite	2.1	1.3	1.6	$CaCO_3$	1611066
Halite	0.4	0.4	0.3	NaCl	311644
Phosphammite	1.1	0.9	0.3	$H(NH_4)_2(PO_4)$	1401715
Corundum	0.7	0.6	0.4	Al_2O_3	527601
Goethite	0.4	0.5	0.3	FeO(OH)	71810
Gibbsite	0.2	0.2	0.2	$Al(OH)_3$	1005040
Iron	0.1	0.1	0.1	Fe	1503158
Natrite	–	2.3	4.7	Na_2CO_3	168130
Amorphous phase	68.1	67.3	68.5	–	–
Sum	100	100	100	–	–

[a] The compositional data for MBA is sourced from our previous publication [27].

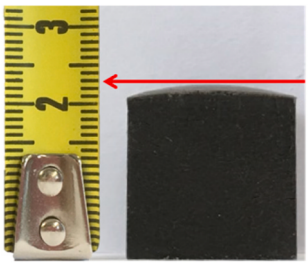

Fig. 12. Side view of 1-day 10 MBA-BFS AAM paste sample.

explained by the comparable reactivity of MBA and FA used in this study [27].

The higher 28-day compressive strength of 20 CMBA-BFS AAM and 30 CMBA-BFS AAM is most likely due to MBA reacting with the activator before the addition of BFS. The NaOH solution treatment and pre-activation process accelerated the reaction of MBA, contributing to strength development within the first 28 days. In the case of FA-BFS AAM, the FA and BFS were mixed with the activator at the same time. The reaction rate of FA at room temperature is very slow and usually contributes to the strength development at later ages [55,70]. The contribution of FA to the 28-day compressive strength was much lower

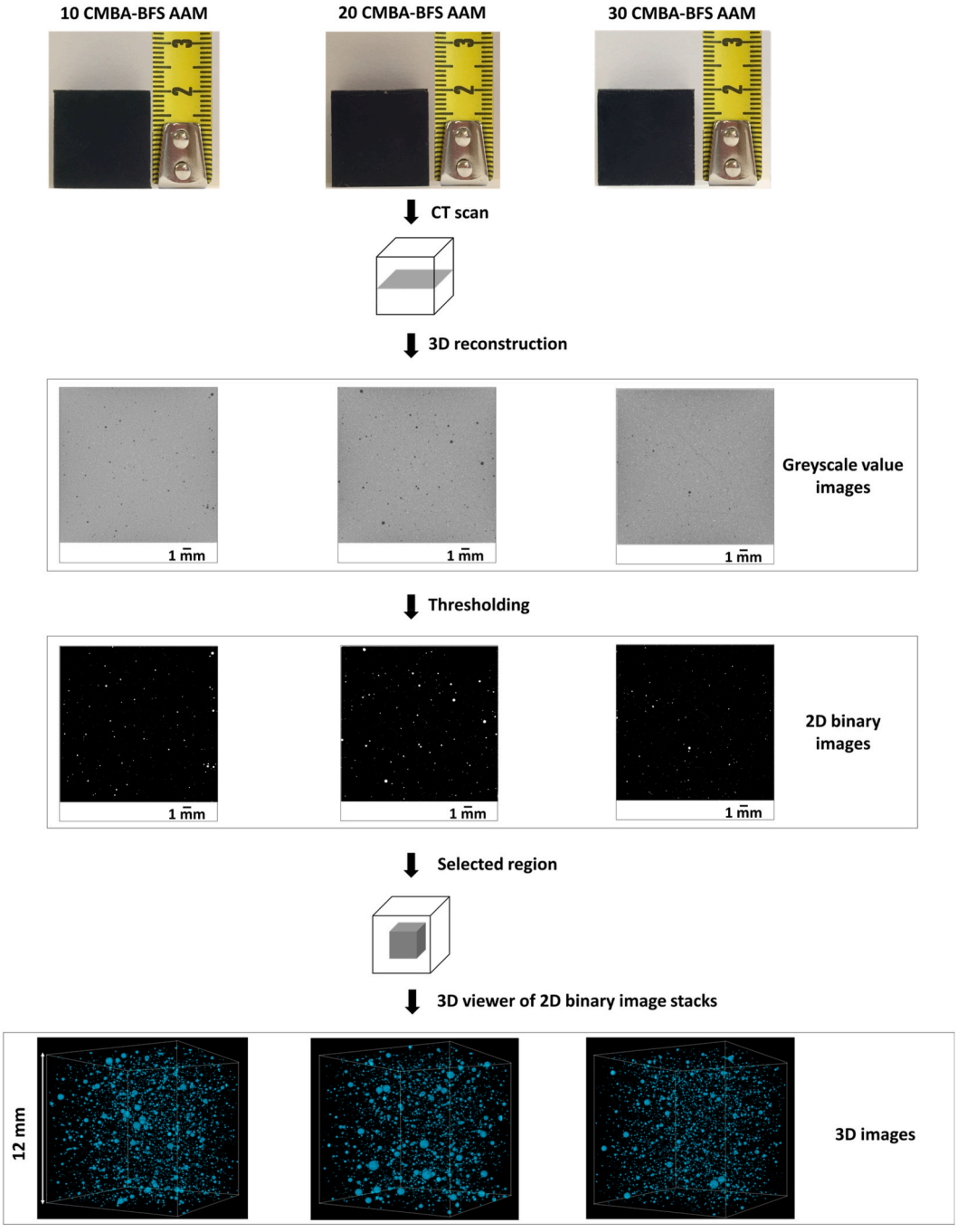

Fig. 13. CMBA-BFS AAM paste samples: Photos of 1-day CMBA-BFS AAM paste samples show no visible evidence of volume expansion. The greyscale value images, two-dimensional (2D) binary images, and three-dimensional (3D) images reveal the presence of internal pores. The pores are represented by white areas in the 2D binary images. The cyan-colored regions in the 3D images indicate pore space. (For interpretation of the references to color in this figure legend, the reader is referred to the Web version of this article.)

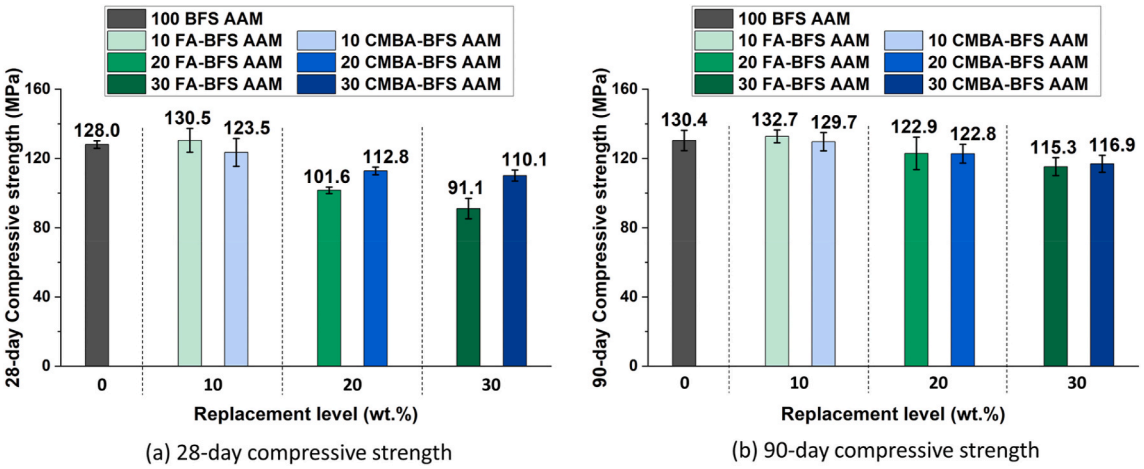

Fig. 14. (a) 28-day and (b) 90-day compressive strength of alkali-activated pastes.

than its contribution to the 90-day compressive strength.

3.3. Microstructure development of alkali-activated pastes

In the following section, the alkali-activated paste sample prepared with the highest dosage of MBA (30 CMBA-BFS AAM) is analyzed to evaluate the effects of the NaOH solution treatment, the pre-activation process, and MBA incorporation on microstructure development.

3.3.1. Reaction kinetics

In the heat evolution curves (Fig. 15 (a)), the main peaks observed between 0.5 and 1 day correspond to reaction product formation. Since BFS exhibits higher reactivity than CMBA and M300, its reaction contributes the most to reaction product formation and heat release during the initial stage. The lower exotherms and cumulative heat release (Fig. 15 (b)) observed in 30 CMBA-BFS AAM and 30 M300-BFS AAM, compared to 100 BFS AAM, are attributed to the reduced BFS content in the binary AAM system. When comparing 30 CMBA-BFS AAM and 30 M300-BFS AAM, the main peak in 30 CMBA-BFS AAM is less intense, and its cumulative heat generation is also lower, indicating a lower reaction degree of BFS within the first 7 days.

Fig. 15 (a) shows that the main peak of 30 CMBA-BFS AAM is significantly delayed, appearing later than the peaks of 100 BFS AAM and 30 M300-BFS AAM. The extension of the induction period in 30 CMBA-BFS AAM is due to the delay of the BFS reaction. There are three factors contributing to this delay. First, the Ca, Si, and Al dissolved from MBA during the NaOH solution treatment increased the concentrations of these ions in the activator, which can inhibit the dissolution of BFS. Second, the pH of the activator decreased after its consumption during the NaOH solution treatment and the pre-activation process. A lower pH in the activator leads to a slower dissolution of BFS. Third, before adding BFS, the pre-activation of CMBA had already consumed some of the silicate monomers in the activator. These monomers are the most reactive silicate species essential for gel formation [71]. The lower availability of monomers also results in a slower rate of gel formation.

The slight extension of the induction period in 30 M300-BFS AAM can also be attributed to the delayed reaction of BFS, but the underlying reason differs from that in 30 CMBA-BFS AAM. The same activator was used to prepare 30 M300-BFS AAM and 100 BFS AAM (see Table 1). Since M300 does not consume activator, a larger portion of the activator remains available to react with the BFS in 30 M300-BFS AAM. The presence of silicate species in the activator can reduce the chemical driving force for dissolving additional silicate species from BFS.

3.3.2. Reaction degree of BFS at 90 days

After 90 days, the reaction degree of BFS is higher in 30 CMBA-BFS AAM and 30 M300-BFS AAM compared to that in 100 BFS AAM (see Fig. 16). This increased reaction degree in the binary system can be explained by the heterogeneous nucleation and dilution effects of CMBA and M300. The CMBA and M300 particles can serve as nucleation sites for the heterogeneous precipitation of gel phases [72,73]. Due to the partial substitution of BFS, the activator to BFS mass ratio in 30

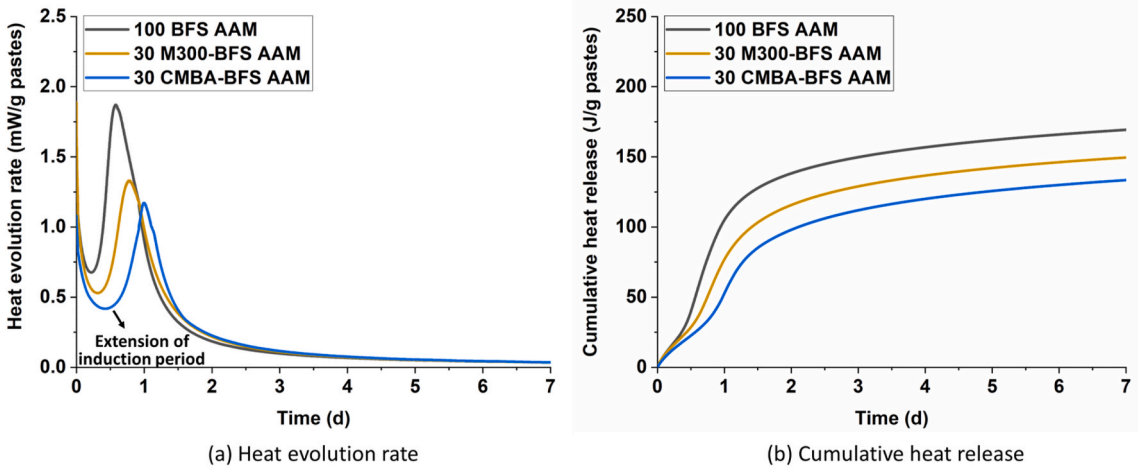

Fig. 15. (a) Heat evolution rate and (b) cumulative heat release per gram of pastes for 100 BFS AAM, 30 M300-BFS AAM, and 30 CMBA-BFS AAM.

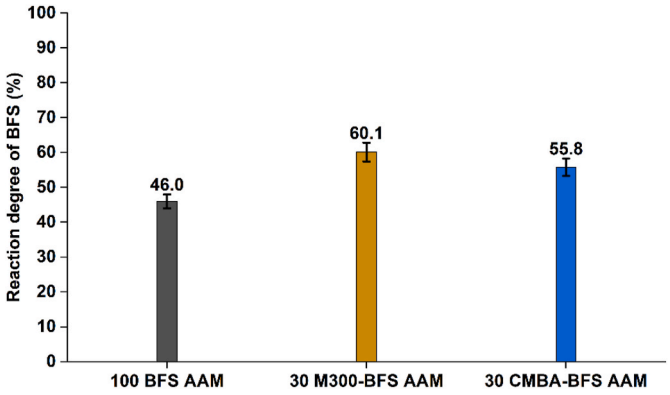

Fig. 16. Reaction degree of BFS in 90-day 100 BFS AAM, 30 M300-BFS AAM, and 30 CMBA-BFS AAM.

CMBA-BFS AAM and 30 M300-BFS AAM is higher than that in 100 BFS AAM, which could promote the activation of BFS.

The accelerating effect of CMBA on the reaction of BFS is less significant than that of M300. In 30 M300-BFS AAM, M300 remained inert and did not consume activator. In the case of 30 CMBA-BFS AAM, a portion of the activator was consumed by MBA during its treatment. CMBA also reacted with the activator during the pre-activation process and the curing phase. Therefore, the slightly lower reaction degree of BFS in 30 CMBA-BFS AAM, compared to 30 M300-BFS AAM, can be attributed to the reduced availability of activator for reaction with BFS.

3.3.3. Crystalline reaction products formed in hardened alkali-activated pastes

The XRD analysis results indicate that the crystalline reaction products formed in 30 CMBA-BFS AAM are tobermorite ($Ca_{4.9}(Si_{5.5}Al_{0.5}O_{16.3})(OH)_{0.7}(H_2O)_5$, ICSD code 93590) and hydrotalcite ($Mg_{0.667}Al_{0.333}(OH)_2(CO_3)_{0.167}(H_2O)_{0.5}$, ICSD code 81963). These two phases are also present in the reference samples (100 BFS AAM and 30 M300-BFS AAM). Tobermorite is identified in XRD analysis because the C-A-S-H gel formed in BFS-based AAM can develop a tobermorite-type structure [74]. Brucite ($Mg(OH)_2$, ICSD code 28275) was only detected in the reference samples, with a peak at 2θ of 38° (see Figs. 19 and 20).

In the XRD patterns of 30 CMBA-BFS AAM, the peaks of tobermorite, albeit overlapping with the peaks of quartz, are evident at 2θ of 49.5° (Fig. 17). The peaks of the tobermorite are less noticeable in the XRD spectra of 30 M300-BFS AAM than in 30 CMBA-BFS AAM, as these peaks overlap with the amorphous hump and the peaks of quartz (Fig. 20). For ease of comparison, the fitted curves of the tobermorite obtained after the Rietveld refinement were demonstrated together with the XRD patterns of 30 CMBA-BFS AAM and 30 M300-BFS AAM.

The hydrotalcite peaks were only observed at 2θ of 11.5° in the XRD patterns of 30 CMBA-BFS AAM (Fig. 18). Comparatively, more hydrotalcite peaks were identified in the XRD spectra of 100 BFS AAM and 30 M300-BFS AAM, with higher peak intensities. The peaks of hydrotalcite were found at 2θ of 11.5°, 23.2°, and 61° in the XRD spectra of 100 BFS AAM (Fig. 19). In the XRD patterns of 30 M300-BFS AAM, the peaks of hydrotalcite appeared at the same locations as those in 100 BFS AAM (Figs. 20 and 21).

The QXRD analysis results show that 30 CMBA-BFS AAM contains a higher amount of tobermorite but a lower amount of hydrotalcite than 30 M300-BFS AAM (see Fig. 22). This difference can be linked to the C-A-S-H gel formed during the sample preparation process of 30 CMBA-BFS AAM (see section 3.1). Due to the pre-existence of C-A-S-H gel, aluminum species dissolved from BFS are more likely to incorporate into the gel rather than contribute to hydrotalcite precipitation during the curing period [75]. Additionally, replacing BFS with MBA decreases the overall MgO content, which further limits hydrotalcite formation [27,74]. An increase in the C-A-S-H gel formation raised the likelihood of detecting tobermorite in XRD analysis. The development of C-A-S-H gel with a tobermorite-like structure over time is driven by Al incorporation and increased crosslinking within the silicate network. [74]. In 30 M300-BFS AAM, there is no pre-existing C-A-S-H gel to promote its

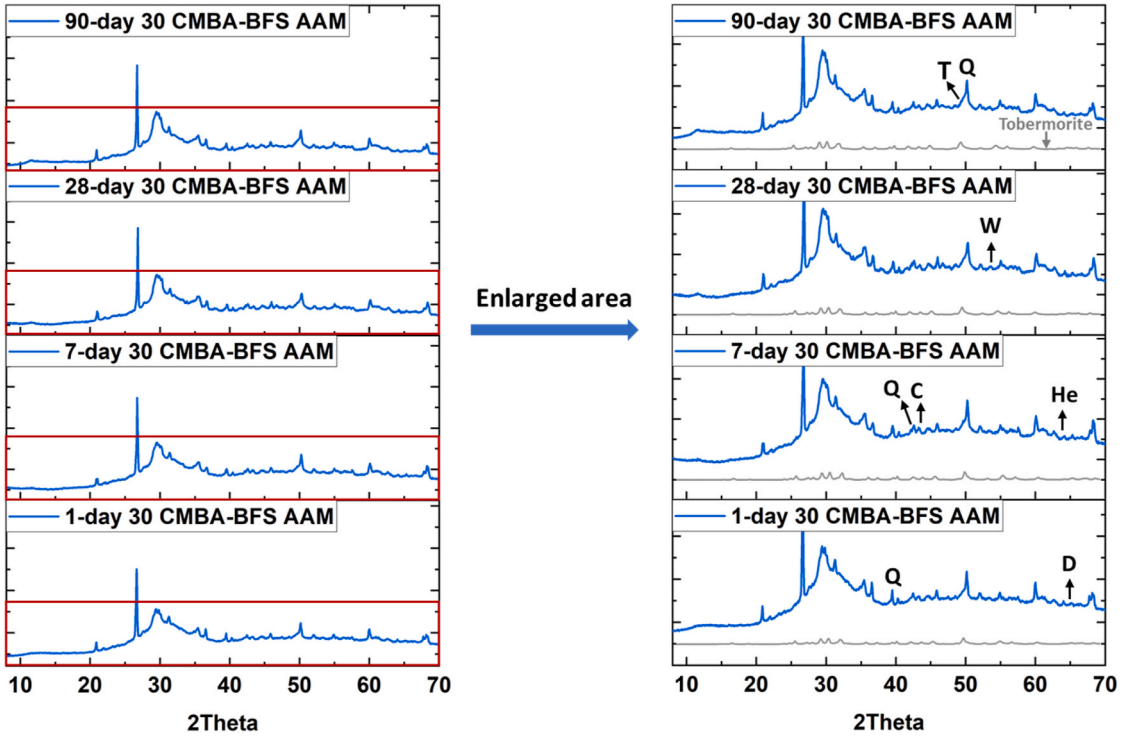

Fig. 17. XRD patterns of 30 CMBA-BFS AAM at different curing ages (enlargement of low-intensity peaks). Q: Quartz, T: Tobermorite, W: Wollastonite, He: Hematite, D: Diopside, C: Calcite. The fitted pattern of tobermorite is obtained after Rietveld refinement.

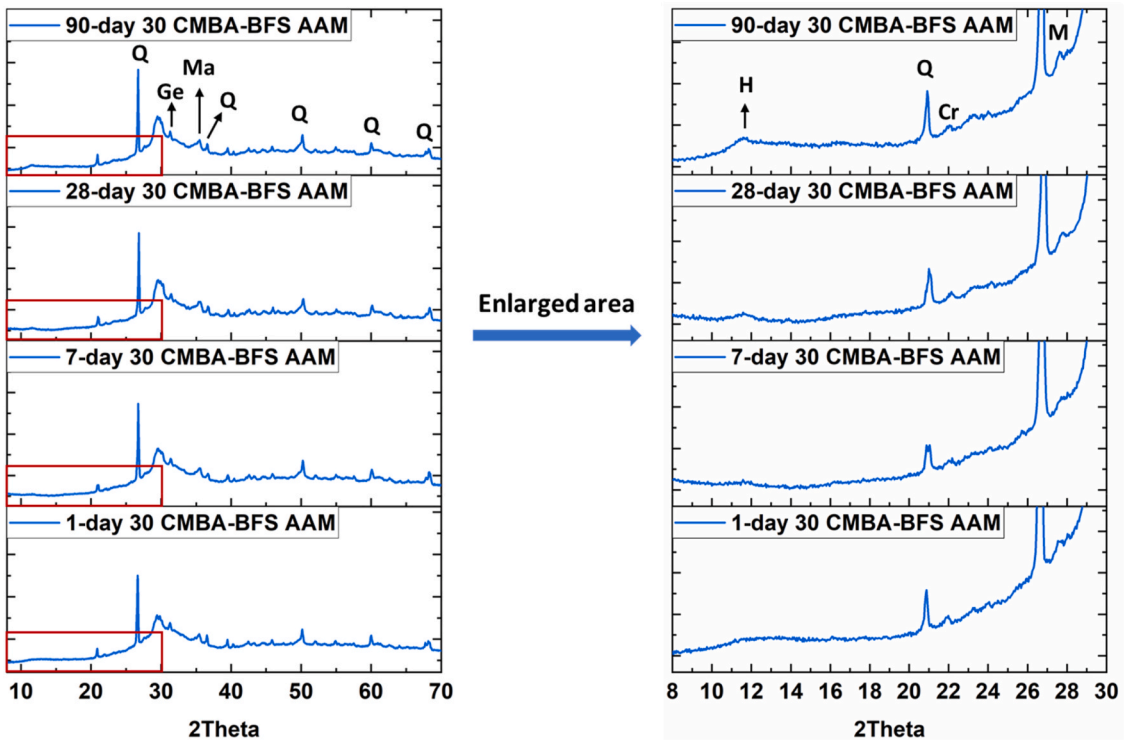

Fig. 18. XRD patterns of 30 CMBA-BFS AAM at different curing ages (enlargement of low-angle area). Q: Quartz, H: Hydrotalcite, Cr: Cristobalite, Ge: Gehlenite, Ma: Magnetite, M: Microcline.

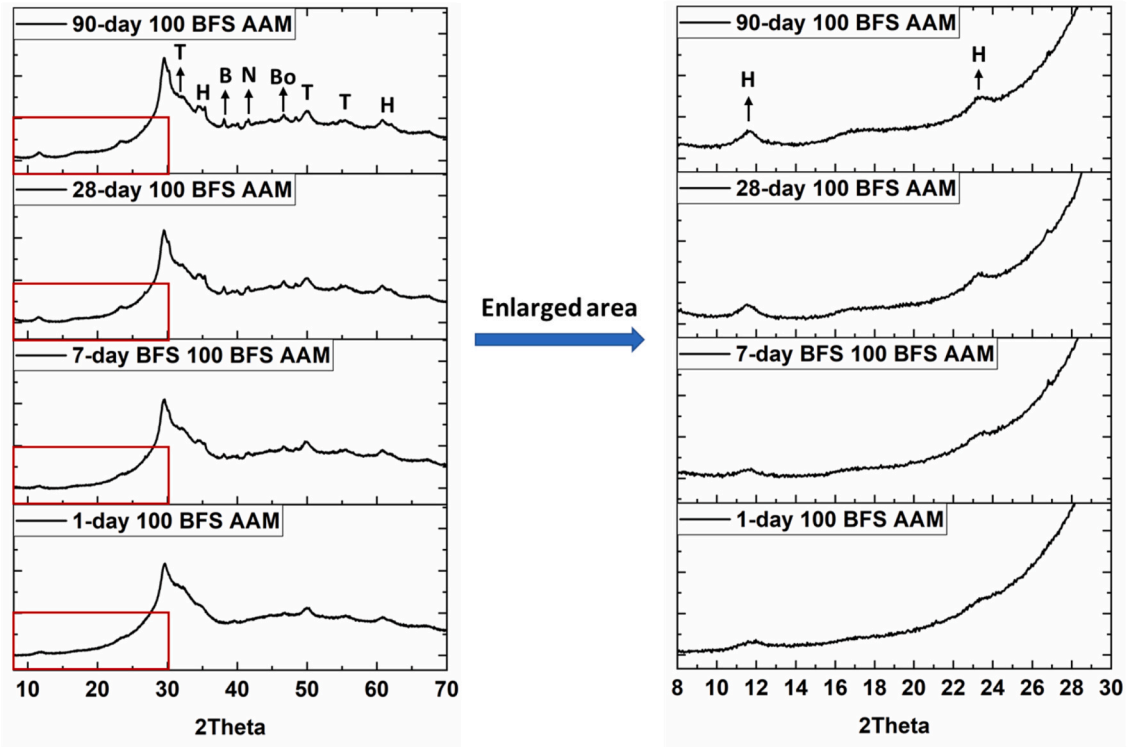

Fig. 19. XRD patterns of 100 BFS AAM at different curing ages. H: Hydrotalcite, T: Tobermorite, B: Brucite, N: Nickel titanium, Bo: Bornite.

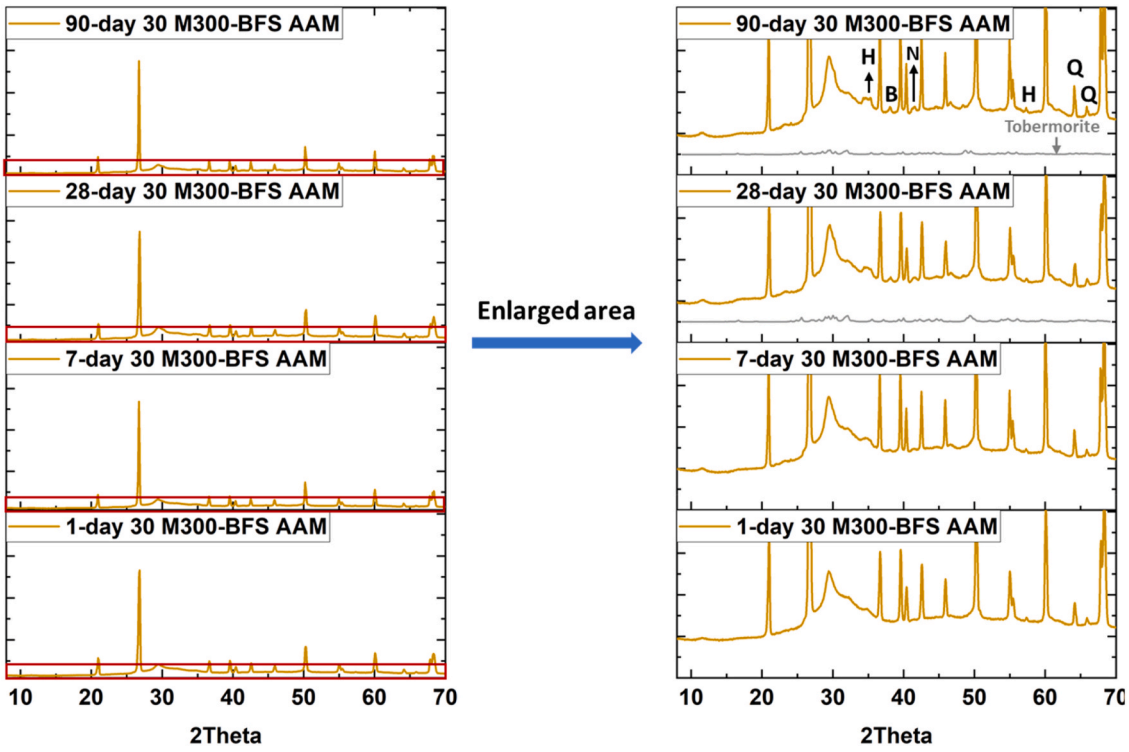

Fig. 20. XRD patterns of 30 M300-BFS AAM at different curing ages (enlargement of low-intensity peaks). Q: Quartz, H: Hydrotalcite, B: Brucite, N: Nickel titanium. The fitted pattern of tobermorite is obtained after Rietveld refinement.

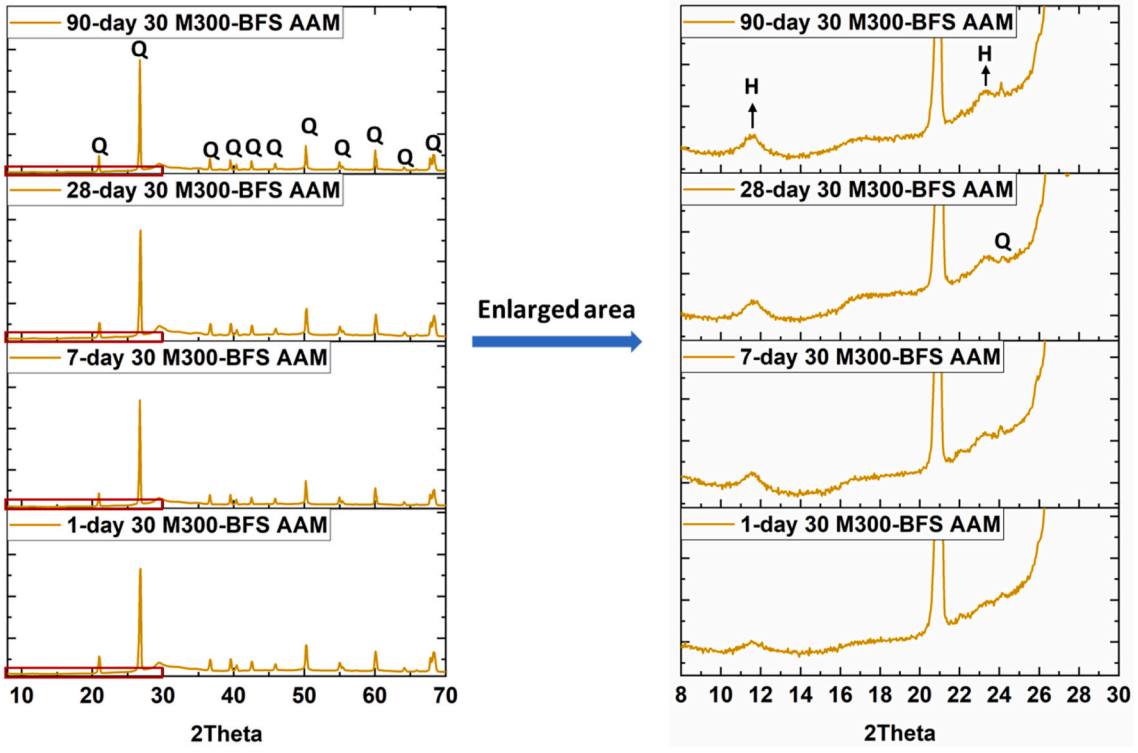

Fig. 21. XRD patterns of 30 M300-BFS AAM at different curing ages (enlargement of low-angle area). Q: Quartz, H: Hydrotalcite.

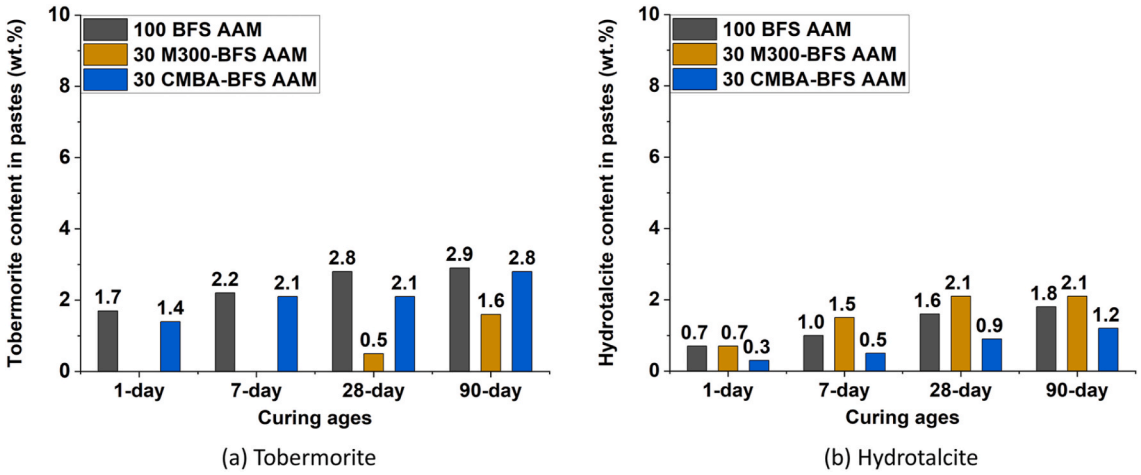

Fig. 22. Tobermorite and hydrotalcite contents determined by QXRD analysis in 100 BFS AAM, 30 M300-BFS AAM, and 30 CMBA-BFS AAM at different curing ages. Data for this figure are provided in Appendix Table 1, Appendix Table 2, and Appendix Table 3.

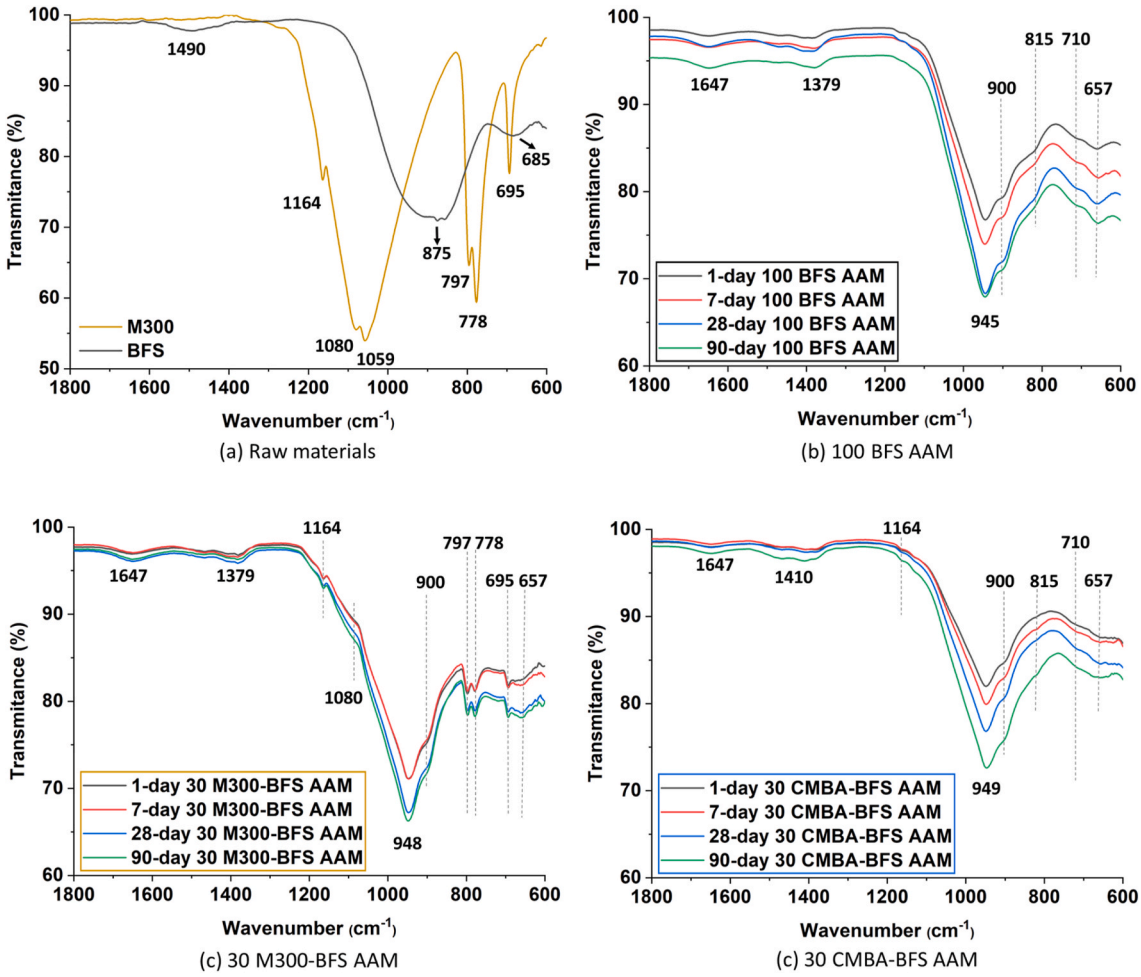

Fig. 23. FTIR spectra of (a) BFS and M300, (b) 100 BFS AAM, (c) 30 M300-BFS AAM, (d) 30 CMBA-BFS AAM. The FTIR spectra of alkali-activated pastes are presented as a function of curing ages.

further formation. The reaction degree of BFS is higher in 30 M300-BFS AAM than in 100 BFS AAM and 30 CMBA-BFS AAM. The higher reaction degree of BFS results in more Mg being released. Before being incorporated in C-S-H gel, the available Al would first combine with Mg to form hydrotalcite [76], as the formation of hydrotalcite-like phases is thermodynamically favored over C-A-S-H gel [77,78].

3.3.4. Chemical bonds in hardened alkali-activated pastes

Fig. 23 presents the FTIR measurement results for alkali-activated pastes, M300, and BFS. The band assignments for these FTIR spectra are provided in Table 4. The main band of BFS, which overlaps with the carbonate band (at 875 cm^{-1}), is broad and centered at around 901 cm^{-1} (Fig. 23 (a)). This band is associated with the asymmetric

Table 4
Band assignments for FTIR spectra of BFS, M300, and alkali-activated pastes shown in Fig. 23.

Wavenumber (cm^{-1})	Assignment	Description
1647	Bending vibration of H-OH [60]	Bond within gel phases.
1300-1500, 875, 685	Vibration of C-O [64,65,80]	Bonds in carbonates
1164, 1080, 1059, 797, 778, 695	Vibrations of Si-O [64]	Characteristic bonds in quartz
945, 948, 949, 893	Stretching vibration of Si-O-T (T: Si, Al, or Na^+) [58–60,67]	Bonds in C-(N-)A-S-H gel
900	Stretching vibration of Si-O [81]	Bonds in tobermorite
657	Bending vibration of Si-O-Si [81]	
815	Symmetric stretching vibrations of Si-O [58]	Bond in the reaction products of alkali-activated slag
710	Bending vibration of Al-O-Si [82,83]	Bond within gel phases.

stretching vibration mode of Si-O-T bonds (T: tetrahedral Si or Al) [79]. Upon alkali activation of BFS, the main band becomes sharper and shifts to a higher wavenumber in the FTIR spectra of 100 BFS AAM (Fig. 23 (b)).

The incorporation of MBA or M300 in BFS-based AAM primarily affected the location of the main band. As illustrated in Fig. 23, the main bands of 30 CMBA-BFS AAM, 30 M300-BFS AAM, and 100 BFS AAM appear at 949 cm^{-1}, 948 cm^{-1}, and 945 cm^{-1}, respectively. The main band of alkali-activated pastes (at around 950 cm^{-1}) can be assigned to the asymmetric stretching vibration of Si-O-T bonds (T: Si, Al, or Na^+) in C-(N-)A-S-H gel (sodium-incorporated C-A-S-H gel) [58–60,67]. These bands did not shift with extended curing time. However, their intensity increased from 1-day to 90-day samples, indicating the continuous formation of C-(N-)A-S-H gel.

The main band in 30 CMBA-BFS AAM appeared at the highest wavenumber, suggesting that the polymerization degree of the gel phases in 30 CMBA-BFS AAM is higher than 100 BFS AAM and 30 M300-BFS AAM. The increased polymerization degree observed in 30 CMBA-BFS AAM is mainly caused by the addition of MBA. The C-A-S-H gel formed from the reaction of MBA during the sample preparation process may enhance the polymerization of gel phases in 30 CMBA-BFS AAM. This effect is evidenced by the detection of a greater amount of tobermorite-type gel compared to that in 30 M300-CMBA AAM (see section 3.3.3). As a SiO_2-rich precursor, CMBA contributes to the formation of Si–O–Si bonds by releasing silicate monomers during the curing process. The Si-O-T bond will shift to a higher wavenumber with an increase in the percentage of the Si-O-Si bonds [58,66]. Moreover, adding MBA to the BFS-based AAM system resulted in gel phases with a lower Ca/Si molar ratio (see Table 5). As the Ca/Si ratio decreases, the silicate chains in the structure become more polymerized, resulting in stronger Si-O bonds and a more ordered structure, which is detected as a shift toward higher wavenumbers in infrared spectroscopy [81].

Table 5
Atomic ratios of the elements present in the gel phases of 90-day 100 BFS AAM, 30 M300-BFS AAM, and 30 CMBA-BFS AAM.

Atomic ratio	100 BFS AAM		30 M300-BFS AAM		30 CMBA-BFS AAM	
	Average	Stdev	Average	Stdev	Average	Stdev
Ca/Si	0.91	0.06	0.73	0.12	0.77	0.11
Al/Si	0.32	0.08	0.29	0.08	0.33	0.08
Na/Si	0.44	0.08	0.47	0.1	0.39	0.08
Mg/Si	0.21	0.09	0.22	0.12	0.21	0.09

3.3.5. Morphology of hardened alkali-activated pastes

Fig. 24 shows representative SEM-BSE images of 90-day 30 CMBA-BFS AAM. To illustrate the differences, images of 90-day 100 BFS AAM and 30 M300-BFS AAM are presented in the same figure. In the SEM-BSE images, the pores filled with epoxy are black. The images acquired at 1500 × magnification indicate that the microstructure of 100 BFS AAM (Fig. 24 (a)) is denser than that of 30 M300-BFS AAM (Fig. 24 (c)) and 30 CMBA-BFS AAM (Fig. 24 (e)), as fewer pores are visible.

Fig. 24(b)–(d) and (f) provide high magnification views (4000 ×) of the BFS, M300 and CMBA particles, along with their surrounding areas. The BFS, M300, and CMBA particles with irregular polygonal shapes are distributed throughout the gel phases. The gel phases generally show a darker grey color than the embedded particles. However, the grey level of M300 particles is close to that of the gel matrix. The BFS and M300 particles both exhibit uniform grey levels in the SEM-BSE image. In contrast, variations in grey levels can be observed within a single CMBA particle, which suggests compositional heterogeneity.

The homogeneous composition of BFS ensures that all the particles are reactive. The partially and completely reacted BFS particles exhibit characteristic features in the SEM-BSE images of alkali-activated pastes. As can be observed in Fig. 24(b)–(d), and (f), the reaction products formed rims along the edges of the partially reacted BFS particles. The BFS particles that had entirely reacted left regions with a darker grey-scale value than the surrounding gel phases. These regions are usually in the shape of the original BFS particles (see Fig. 24 (b)).

The CMBA particles have a heterogeneous composition, resulting in only certain particles being reactive. The partially reacted CMBA particles show distinct features in the SEM-BSE images, with a layer of reaction products around their edges. Fig. 25 (a) and (b) present two representative examples of partially reacted CMBA particles found in 90-day 30 CMBA-BFS AAM. The layer of reaction products on particles 1 and 2 appears lighter in grey relative to the surrounding gel phases. The thickness of the reaction product layer is around 0.55 μm, which is about half the thickness of the reaction product rim on the BFS particle adjacent to particle 2. It is difficult to accurately determine the elemental composition of the reaction product layers with SEM-EDS spot analysis. The reason is that the electron beam generated at an accelerating voltage of 15 kV interacts not only with the layer but also with the surrounding materials [84].

The reaction product layers were most likely formed due to the chemical reaction between CMBA particles and the pore solution in 30 CMBA-BFS AAM. However, the gel phases formed during the NaOH solution treatment and pre-activation process may also precipitate on the surfaces of CMBA particles. As indicated in section 3.1, the C-A-S-H gel was detected after the NaOH solution treatment and the pre-activation process. During the curing process of 30 CMBA-BFS AAM, the ions dissolved from particles 1 and 2 may promote the accumulation of the gel initially precipitated on their surfaces, leading to the formation of a reaction product layer.

The reactive CMBA particles found in 90-day 30 CMBA-BFS AAM are mainly composed of waste glass. The elemental composition of these particles was determined by SEM-EDS spot analysis, with the primary elements identified as O, Si, Ca, Na, Al, Fe, and Mg. (see Fig. 25 (c)). Although the measurements were taken at specific locations, they are considered indicative of the overall compositions of particles 1 and 2. The grey levels at locations 1 and 2 closely match those in the major regions of each particle. The atomic percentages of Si, Ca, Na, Al, and Fe at locations 1 and 2 and within glass particles in MBA were projected onto the ternary diagrams to visualize their relative contents. In the ternary diagram (Fig. 26), the points corresponding to the measurements taken at locations 1 and 2 fall within the same region as those representing the glass particles in the MBA. This finding also supports the conclusion from our previous work that waste glass is the primary source of the reactive phases in MBA [27].

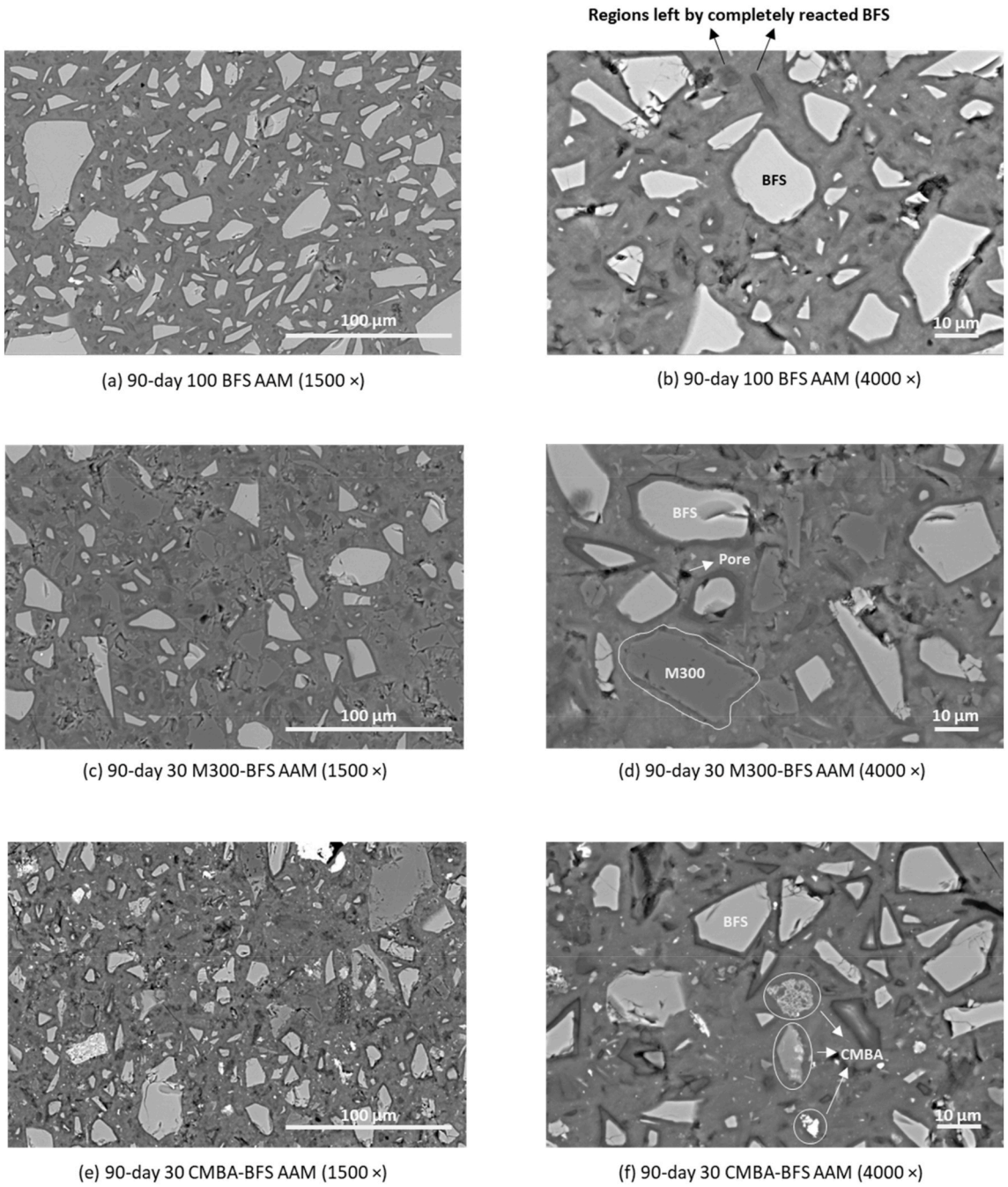

Fig. 24. SEM-BSE images of 90-day 100 BFS AAM, 30 M300-BFS AAM, and 30 CMBA-BFS AAM paste samples captured at 1500x and 4000x magnifications.

3.3.6. Chemical composition of the gel phases in alkali-activated pastes

The chemical compositions of the gel phases formed in 90-day 30 CMBA-BFS AAM, 100 BFS AAM, and 30 M300-BFS AAM are compared to identify the changes induced by the addition of MBA. The gel compositions were plotted on the ternary diagram, with each point representing the proportions of three elements. In Fig. 27, the Al, Si, Ca, and Na atomic percentages are presented on an oxide basis and plotted in the CaO - Al_2O_3 - SiO_2 and Na_2O - Al_2O_3 - SiO_2 ternary diagrams after renormalizing to 100 %.

Fig. 27 shows an overlap in data points within the ternary diagram, suggesting compositional similarity among the gels of 30 CMBA-BFS AAM, 30 M300-BFS AAM, and 100 BFS AAM. The data points cluster in a region characterized by high SiO_2 and CaO but low Al_2O_3 and Na_2O percentages. This distribution indicates that the C-(N-)A-S-H gel is the primary component in the gel matrix. Given the high CaO content in BFS, the significant proportion of BFS in the precursors of 30 CMBA-BFS AAM, 30 M300-BFS AAM, and 100 BFS AAM results in all three systems being classified as Ca-rich. In Ca-rich AAM systems, the C-(N-)A-S-H gel is typically recognized as the main reaction product [77].

The ternary diagram reveals the presence of C-A-S-H gel in the binary AAM systems. On the Na_2O - Al_2O_3 - SiO_2 ternary diagram, several data points representing the gel compositions of 30 CMBA-BFS AAM and 30 M300-BFS AAM are located near the top vertex, where the Na_2O percentage is zero (Fig. 27 (b)). These points correspond to the regions within the gel matrix where sodium was rarely detected. This observation suggests the presence of C-A-S-H gel, which is further supported by the detection of tobermorite in the XRD analysis of 30 CMBA-BFS AAM and 30 M300-BFS AAM.

On the CaO - Al_2O_3 - SiO_2 ternary diagram, some points are located in a region where CaO is nearly absent, indicating the presence of N-A-S-H

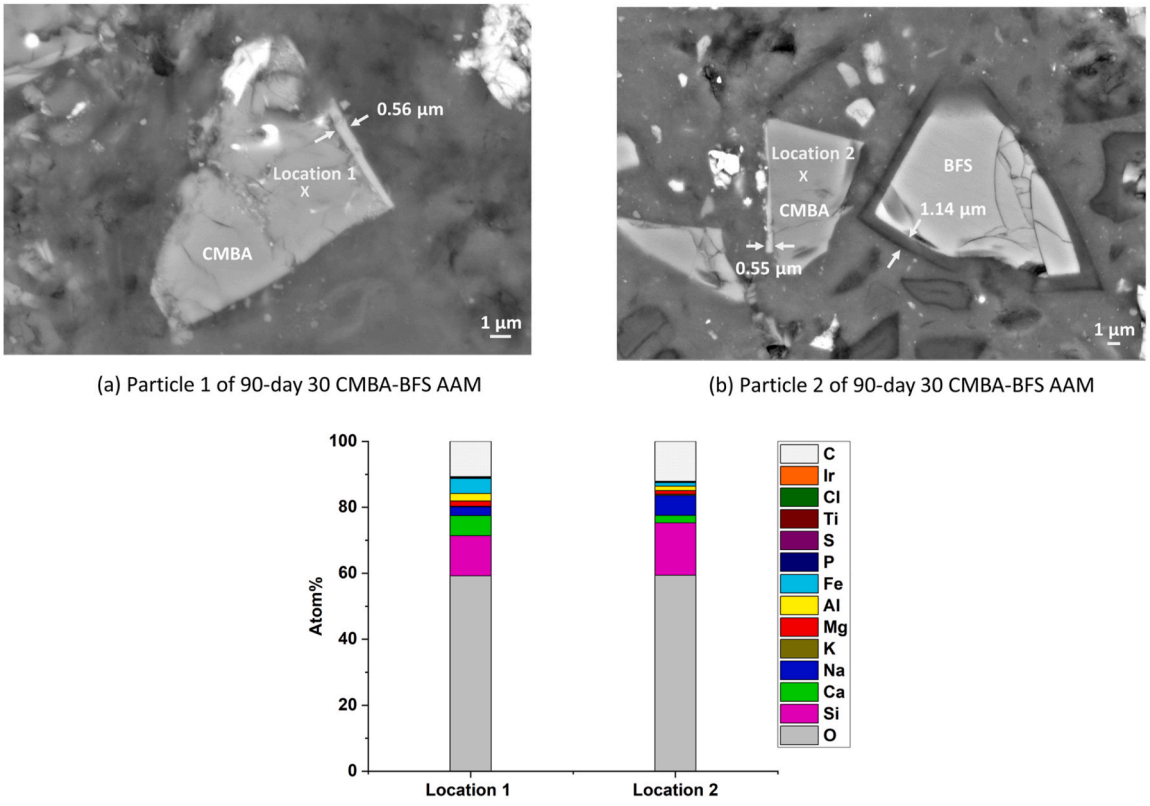

(a) Particle 1 of 90-day 30 CMBA-BFS AAM

(b) Particle 2 of 90-day 30 CMBA-BFS AAM

(c) Chemical compositions of the locations in particle 1 and particle 2 of 90-day 30 CMBA-BFS AAM

Fig. 25. (a) and (b) SEM-BSE images of partially reacted CMBA particles found in 90-day 30 CMBA-BFS AAM. (c) SEM-EDS spot analysis results from the marked locations in these particles.

gel. However, the content of this gel in 30 CMBA-BFS AAM and 30 M300-BFS AAM should be minimal. When a considerable amount of Ca is present in the pore solution of AAM, the Si and Al are more likely to participate in forming C-A-S-H gel than N-A-S-H gel. The C-A-S-H gel is more stable than the N-A-S-H gel under highly alkaline conditions (pH $>$ 12) [60]. Besides, the Ca released by BFS can partially replace the Na in the N-A-S-H gel, resulting in the formation of (N,C)-A-S-H gel, also called calcium-modified N-A-S-H gel [85].

The average atomic ratios were calculated for the gel phases of the 90-day alkali-activated paste samples. As shown in Table 5, the incorporation of MBA in BFS-based AAM leads to a notable change in the Ca/Si atomic ratio. The Ca/Si atomic ratio (0.91) in the gel of 100 BFS AAM is close to that in the amorphous phase of BFS [27]. Compared with the gel of 100 BFS AAM, the gel formed in 30 CMBA-BFS AAM shows a decreased Ca/Si ratio. A comparable decrease in the Ca/Si ratio is observed in the gel of 30 M300-BFS AAM. The lower Ca/Si ratio of the gel formed in the binary AAM systems can be attributed to the reduced amount of CaO present in these systems.

3.3.7. *Pore characteristics of hardened alkali-activated pastes*

The pore characteristics of 90-day 30 CMBA-BFS AAM were compared with those of 90-day 100 BFS AAM and 30 M300-BFS AAM, focusing on pore volume and pore size distribution. A key feature of AAM is the abundance of nanopores smaller than 100 nm, which significantly influences the pore structure [50]. The nitrogen adsorption test results show that the 90-day 30 CMBA-BFS AAM has the highest nanopore volume, followed by 90-day 30 M300-BFS AAM and 100 BFS AAM (see Fig. 28 (a)). The 90-day 30 CMBA-BFS AAM and 100 BFS AAM both exhibit a peak at 15 nm in the differential pore size distribution curves (see Fig. 28 (b)), suggesting a similar pore size distribution. Comparatively, the 90-day 30 M300-BFS AAM shows a peak at a larger pore size of 20 nm, indicating a coarser pore structure.

The formation of gel reduces macropores (50–200 nm) by filling the gaps between unreacted particles while concurrently increasing the volume of mesopores (3.6–50 nm) [86]. The pore volume in the binary AAM systems is higher because the reaction products available to fill the macropores are less in 30 CMBA-BFS AAM and 30 M300-BFS AAM than in 100 BFS AAM. The higher pore volume observed in 90-day 30 CMBA-BFS AAM compared to 90-day 30 M300-BFS AAM can be explained by considering the factors influencing the pore volumes, including raw material densities, the reaction kinetics of the alkali-activated pastes, and the characteristics of the reaction products. More detailed explanations are presented below.

- The same mass of MBA and M300 was used to prepare 30 CMBA-BFS AAM and 30 M300-BFS AAM, respectively. However, due to the higher density of MBA, it occupies a smaller volume than M300, leading to a higher initial pore volume in 30 CMBA-BFS AAM.
- In the early stages, the reaction of BFS was delayed for a longer time in 30 CMBA-BFS AAM than in 30 M300-BFS AAM (Fig. 15 (a)). This

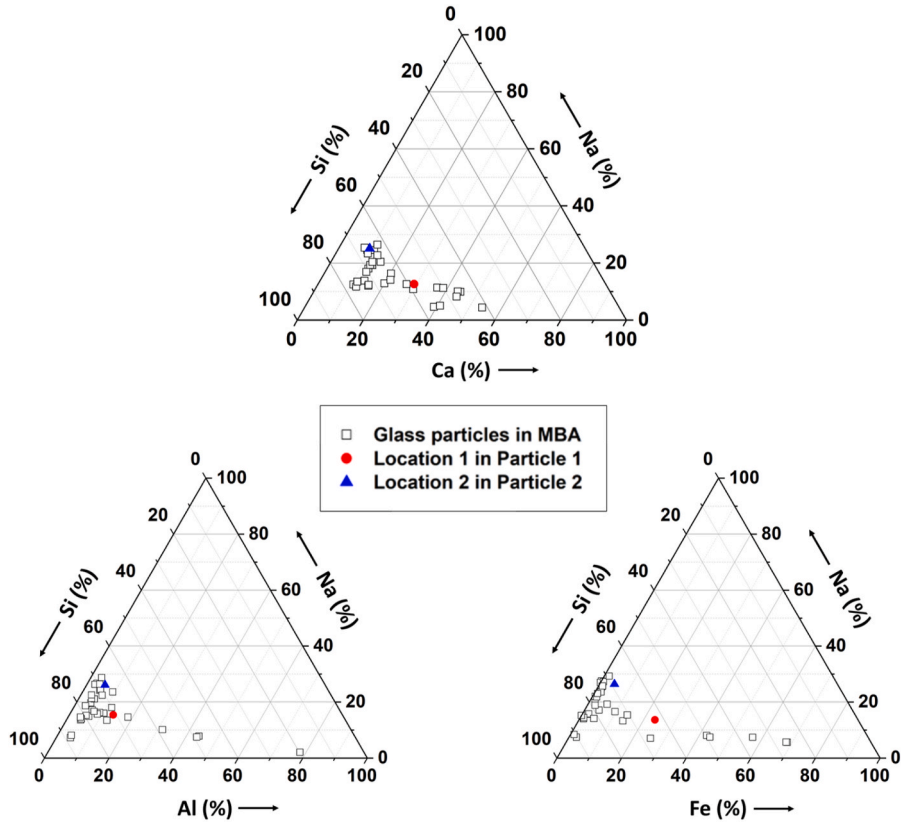

Fig. 26. Ternary diagrams illustrating the relative contents of Si, Ca, Na, Al, and Fe to compare the compositions of particles 1 and 2 in the 90-day 30 CMBA-BFS AAM with the glass particles in MBA. The atomic percentages of these elements were used to plot the diagrams. The compositions of particles 1 and 2 are represented by the data collected at locations 1 and 2, respectively (see Fig. 25).

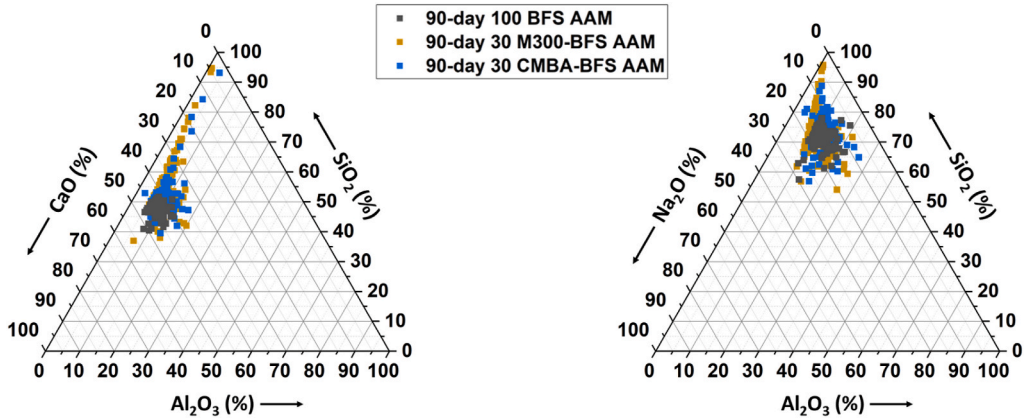

Fig. 27. (a) CaO - Al_2O_3 - SiO_2 and (b) Na_2O - Al_2O_3 - SiO_2 ternary diagrams comparing the main elements present in the gel phases 90-day 100 BFS AAM, 30 M300-BFS AAM, and 30 CMBA-BFS AAM. The diagrams plotted based on the atomic percentages of the oxides.

delay resulted in fewer reaction product formation, leaving the 7-day 30 CMBA-BFS AAM with a higher pore volume than the 7-day 30 M300-BFS AAM. The reaction products formed in 30 CMBA-BFS AAM between 7 and 90 days may not be sufficient to lower its pore volume below that of 30 M300-BFS AAM. One reason is that the pore volume filled by the reaction products of BFS is smaller in 30 CMBA-BFS AAM than in 30 M300-BFS AAM, given the slightly lower reaction degree of BFS in 30 CMBA-BFS AAM after 90 days. The other reason is that the reaction of MBA primarily contributes to gel formation, which reduces macropore volume but increases mesopore volume.

- The hydrotalcite content also affects the pore volume of BFS-based AAM. An equal mass of hydrotalcite occupies a larger volume than the gel formed in alkali-activated BFS pastes due to the lower density of hydrotalcite [76,87]. The amount of hydrotalcite detected in 90-day 30 M300-BFS AAM is greater than in 90-day 30 CMBA-BFS

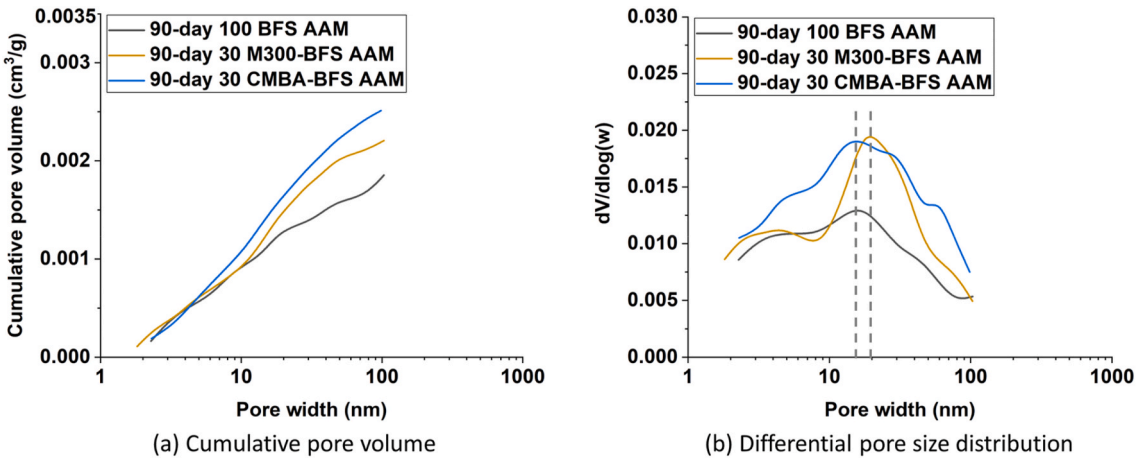

Fig. 28. Cumulative pore volume and differential pore size distribution curves of 100 BFS AAM, 30 M300-BFS AAM, and 30 CMBA-BFS AAM at 90 days, determined by nitrogen adsorption analysis.

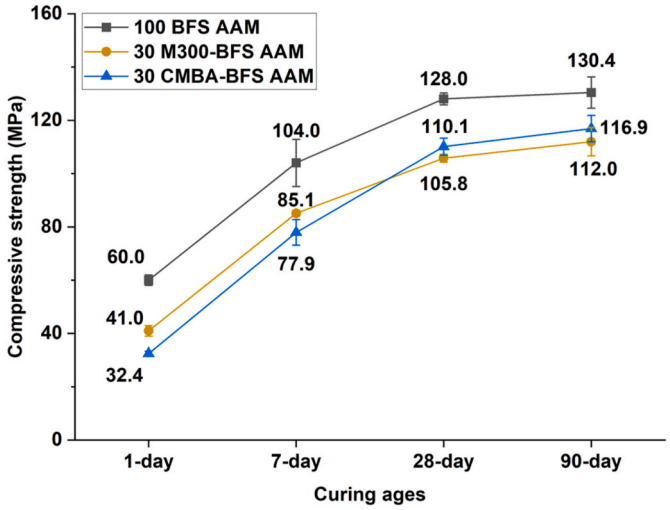

Fig. 29. Compressive strength of 100 BFS AAM, 30 M300-BFS AAM, and 30 CMBA-BFS AAM as a function of curing ages.

AAM. Therefore, hydrotalcite contributed less to pore volume reduction in 30 CMBA-BFS AAM compared to 30 M300-BFS AAM.

3.4. Strength development of hardened alkali-activated pastes

As illustrated in Fig. 29, the incorporation of MBA or M300 into BFS-based alkali-activated pastes led to a decrease in compressive strength, particularly at early ages. The 1-day compressive strength of 100 BFS AAM was 60 MPa. In comparison, the compressive strength of 30 M300-BFS AAM and 30 CMBA-BFS AAM at 1 day was more than 30 % lower. At later stages, the BFS reaction in the binary AAM system was enhanced, with a higher reaction degree compared to the 100 BFS AAM. As a result, the 90-day compressive strength of 30 CMBA-BFS AAM and 30 M300-BFS AAM was only around 10 % and 14 % lower than that of 100 BFS AAM, respectively.

Compared with 30 M300-BFS AAM, the 1-day and 7-day compressive strength of 30 CMBA-BFS AAM is lower. This is because the reaction of BFS was significantly delayed in 30 CMBA-BFS AAM during the first 7 days (see Fig. 15 (a)). After 28 days, the compressive strength of 30 CMBA-BFS AAM increased to 110 MPa, exceeding that of 30 M300-BFS AAM. At 90 days, the 30 CMBA-BFS AAM with a compressive strength of 116 MPa remained stronger than the 30 M300-BFS AAM. Due to the lower reaction degree of BFS, its contribution to the strength development of 90-day 30 CMBA-BFS AAM is smaller than that of 90-day 30 M300-BFS AAM. This indicates that the higher compressive strength of 30 CMBA-BFS AAM at later ages primarily results from the contribution of CMBA to reaction product formation.

4. Conclusions

This study has demonstrated an effective approach for increasing the contribution of MSWI bottom ash (MBA) to reaction product formation, when it is used in blast furnace slag (BFS)-based alkali-activated blends. This work also elucidates the underlying mechanism by studying the microstructure formation and strength development of alkali-activated material (AAM) derived from the blends of BFS and MBA. The insights gained from this research provide a solid foundation for the broader adoption of MBA in AAM production. The findings of this work are detailed below:

- When the pre-treatment and pre-activation processes are incorporated into the sample preparation procedure, the resulting binder material, designated as CMBA-BFS AAM, does not exhibit volume expansion. At 28 days, the compressive strength of CMBA-BFS AAM is notably higher, compared to the AAM made with BFS and Class F coal fly ash (FA). At 90 days, the compressive strengths of both mixtures are comparable. These strength results suggest that MBA is a promising substitute for FA in alkali-activated blends.
- The NaOH solution treatment of MBA primarily facilitates the oxidation of metallic Al and the dissolution of the amorphous phase in MBA. This pre-treatment process also leads to the formation of a trace amount of C-A-S-H gel. During the subsequent pre-activation process, a larger amount of C-A-S-H gel is formed, which later promotes further gel formation in alkali-activated pastes.
- Unlike inert micronized sand (M300), MBA influences the reaction product formation and BFS reaction differently. The reaction of MBA consumes a substantial amount of activator and significantly contributes to the formation of C-A-S-H gel with a tobermorite-type

structure and to late-age strength development. The reaction of BFS is initially delayed in both 30 CMBA-BFS AAM and 30 M300-BFS AAM, with a longer delay in the MBA-containing mixture. After 90 days, the reaction degree of BFS in 30 CMBA-BFS AAM remains lower than in 30 M300-BFS AAM but is higher than in 100 BFS AAM.

- The partially reacted bottom ash particles show distinct features in the SEM-BSE images of 30 CMBA-BFS AAM, with a layer of reaction products around their edges. These reactive bottom particles mainly consist of waste glass. The C-(N-)A-S-H gel formed in 30 CMBA-BFS AAM has a unique elemental composition and a higher polymerization degree than the gels of 100 BFS AAM and 30 M300-BFS AAM.
- While 30 CMBA-BFS AAM exhibits higher compressive strength than 30 M300-BFS AAM after 90 days, its nanopore volume is higher. This discrepancy can primarily be attributed to the significant contribution of MBA to gel formation, the lower reaction degree of BFS, and the lower amount of hydrotalcite formed in the 30 CMBA-BFS AAM. Given that pore structure significantly influences properties like permeability, future work should focus on how these changes influence the long-term performance of AAM containing MBA.

CRediT authorship contribution statement

Boyu Chen: Writing – review & editing, Writing – original draft, Visualization, Methodology, Investigation, Formal analysis, Data curation, Conceptualization. **Guang Ye:** Writing – review & editing, Supervision.

Declaration of competing interest

The authors declare that they have no known competing financial interests or personal relationships that could have appeared to influence the work reported in this paper.

Acknowledgements

Boyu Chen would like to thank the Chinese Scholarship Council for their support for her Ph.D. study. Financial support by Mineralz (Part of Renewi) is acknowledged. Special acknowledgment is given to professor Klaas van Breugel for his help with the improvement of text writing. Dr. Nicola Döbelin from RMS Foundation is gratefully acknowledged for the QXRD analysis. Ruud Hendrix at the Department of Materials Science and Engineering of the Delft University of Technology is acknowledged for the X-ray analysis. Arjan Thijssen, Ton Blom, Maiko van Leeuwen, and John van de Berg from the Stevin lab and Microlab at the Faculty of Civil Engineering and Geosciences, Delft University of Technology, are acknowledged for their support for all the experiments.

Appendix

- **Description of image analysis method to determine reaction degree of BFS in AAM**

According to Chayes et al. [88], the volume fractions can be assumed to be equal to the area fraction calculated from two-dimensional images. The number of frames required for the image analysis was determined according to the method proposed by Ye [54]. The SEM-BSE image used for the image analysis was taken at the magnification of 1500. The frame area of this SEM-BSE image was 50770 μm^2. The area fraction of BFS was plotted as a function of the total investigated area. Appendix Figure 1 indicates that the area fraction of BFS reached a stable value after the total investigated area exceeded 7.6×10^5 μm^2. This means at least fifteen SEM-BSE images were required to get a representative area fraction of BFS in the pastes.

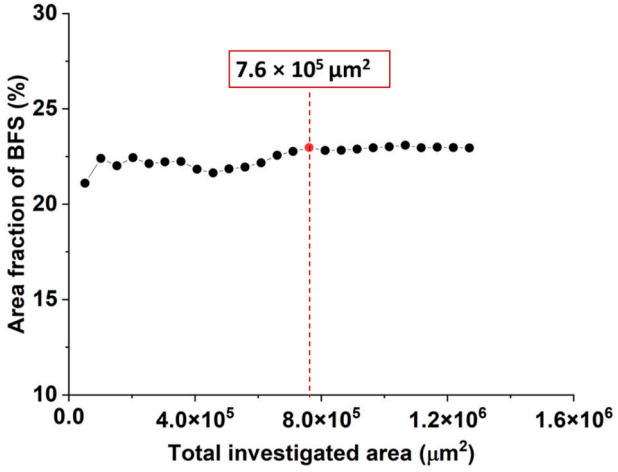

Appendix Fig. 1. The area fraction of blast furnace slag as a function of total investigated area for 90-day 100 BFS AAM paste sample.

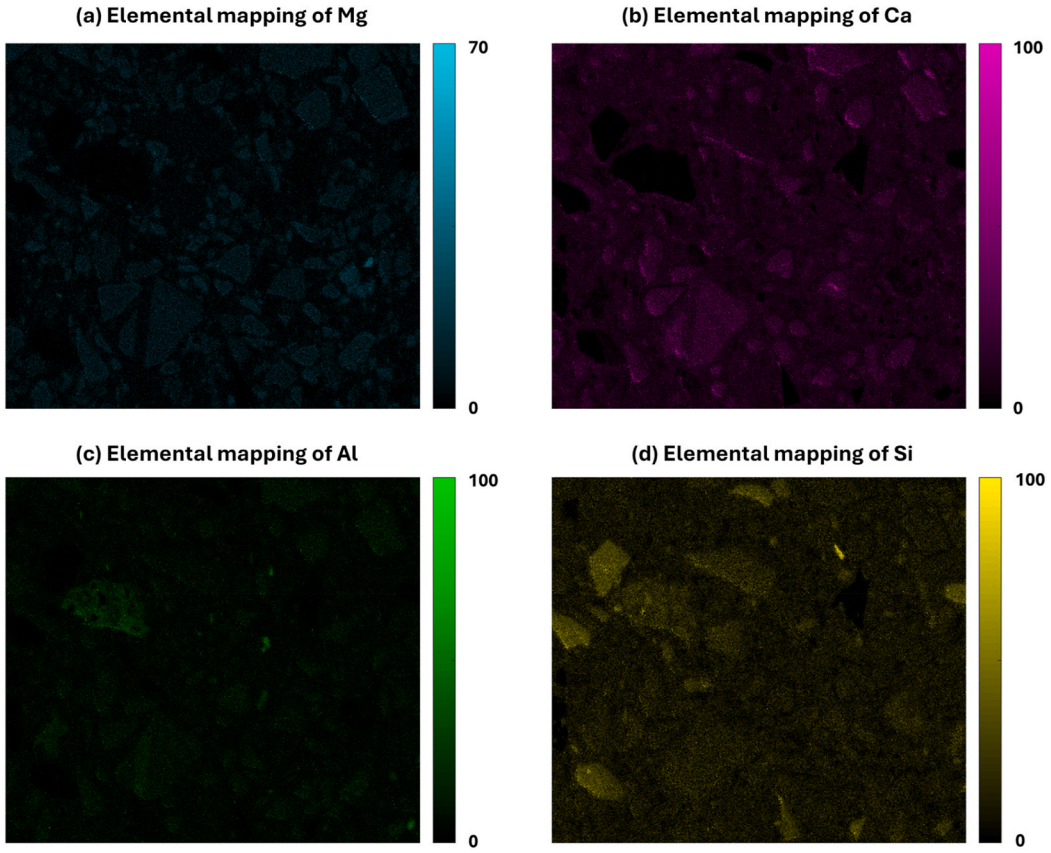

Appendix Fig. 2. SEM-EDS Elemental mappings of Mg, Ca, Al and Si for 90-day 30 CMBA-BFS AAM.

In Appendix Figure 3, the x-axis represents the Ca/Si or Al/Si molar ratio calculated for each particle, while the y-axis shows the number of particles corresponding to each molar ratio. This histogram provides an overview of the range and frequency of the Ca/Si or Al/Si molar ratios within unreacted BFS particles.

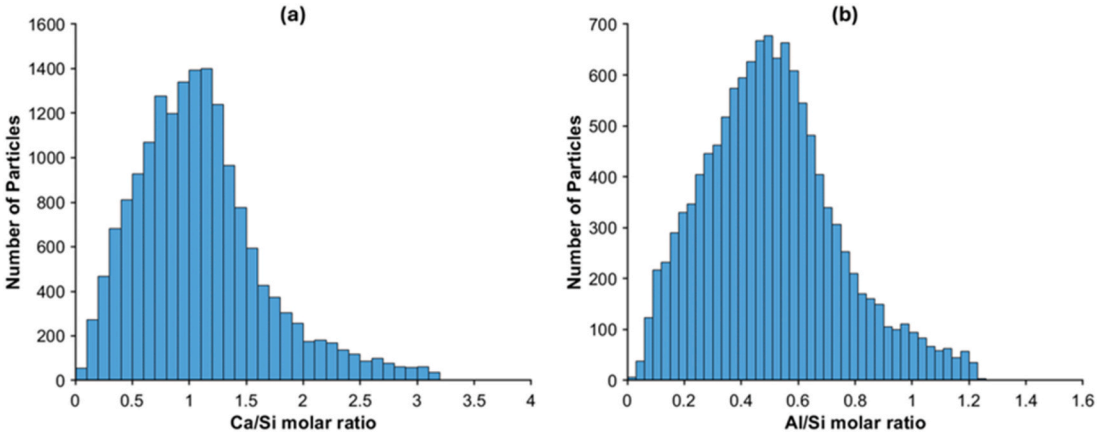

Appendix Fig. 3. Distribution of the Ca/Si and Al/Si molar ratio in unreacted BFS particles.

Appendix Table 1
Composition of mineral phases in 100 BFS AAM after different curing times, determined using QXRD analysis.

Phases (wt.%)	100 BFS AAM			
	1 day	7 days	28 days	90 days
Tobermorite	1.7	2.2	2.8	2.9
Hydrotalcite	0.7	1.0	1.6	1.8

(*continued on next page*)

Appendix Table 1 (*continued*)

Phases (wt.%)	100 BFS AAM			
	1 day	7 days	28 days	90 days
Brucite	–	–	0.4	0.5
Bornite	–	0.1	0.1	0.1
Nickel titanium	–	0.1	0.1	0.1
Amorphous phase	97.6	96.6	95.0	94.6
Sum	100.0	100.0	100.0	100.0

Appendix Table 2
Composition of mineral phases in 30 M300-BFS AAM after different curing times, determined using QXRD analysis.

Phases (wt.%)	30 M300-BFS AAM			
	1 day	7 days	28 days	90 days
Tobermorite	–	–	0.5	1.6
Hydrotalcite	0.7	1.5	2.1	2.1
Brucite	–	–	0.1	0.1
Quartz	27.2	27.2	27.2	27.2
Nickel titanium	–	–	0.1	0.1
Amorphous phase	72.1	71.3	70.0	68.9
Sum	100.0	100.0	100.0	100.0

Appendix Table 3
Composition of mineral phases in 30 CMBA-BFS AAM after different curing times, determined using QXRD analysis.

Phases (wt.%)	30 CMBA-BFS AAM			
	1 day	7 days	28 days	90 days
Tobermorite	1.4	2.1	2.1	2.8
Hydrotalcite	0.3	0.5	0.9	1.2
Microcline	1.1	1.6	1.8	1.9
Quartz	2.8	2.8	2.7	2.3
Cristobalite	0.3	0.3	0.2	0.2
Magnetite	0.3	0.3	0.3	0.3
Hematite	0.2	0.2	0.2	0.2
Gehlenite	1.5	1.5	1.5	1.5
Diopside	1.5	1.4	1.3	1.0
Wollastonite	1.6	1.6	1.6	1.6
Calcite	0.5	0.5	0.5	0.5
Amorphous phase	88.5	87.2	86.9	86.5
Sum	100.0	100.0	100.0	100.0

Data availability

Data will be made available on request.

References

[1] S. Kaza, L. Yao, P. Bhada-Tata, F. Van Woerden, What a Waste 2.0: a Global Snapshot of Solid Waste Management to 2050, The World Bank, 2018.

[2] S.-Y. Pan, M.A. Du, I.-T. Huang, I.-H. Liu, E.-E. Chang, P.-C. Chiang, Strategies on implementation of waste-to-energy (WTE) supply chain for circular economy system: a review, J. Clean. Prod. 108 (2015) 409–421, https://doi.org/10.1016/j.jclepro.2015.06.124.

[3] J.M. Chimenos, M. Segarra, M.A. Fernandez, F. Espiell, Characterization of the bottom ash in municipal solid waste incinerator, J. Hazard Mater. A. 64 (1999) 211–222.

[4] K.L. Lin, D.F. Lin, Hydration characteristics of municipal solid waste incinerator bottom ash slag as a pozzolanic material for use in cement, Cem. Concr. Compos. 28 (2006) 817–823, https://doi.org/10.1016/j.cemconcomp.2006.03.003.

[5] D. Blasenbauer, F. Huber, J. Lederer, M.J. Quina, D. Blanc-Biscarat, A. Bogush, E. Bontempi, J. Blondeau, J.M. Chimenos, H. Dahlbo, J. Fagerqvist, J. Giro-Paloma, O. Hjelmar, J. Hyks, J. Keaney, M. Lupsea-Toader, C.J. O'Caollai, K. Orupõld, T. Pająk, F.G. Simon, L. Svecova, M. Šyc, R. Ulvang, K. Vaajasaari, J. Van Caneghem, A. van Zomeren, S. Vasarevičius, K. Wégner, J. Fellner, Legal situation and current practice of waste incineration bottom ash utilisation in Europe, Waste Manag. 102 (2020) 868–883, https://doi.org/10.1016/j.wasman.2019.11.031.

[6] Y. Tian, A.C. Thanos Bourtsalas, S. Kawashima, S. Ma, N.J. Themelis, Performance of structural concrete using Waste-to-Energy (WTE) combined ash, Waste Manag. 118 (2020) 180–189, https://doi.org/10.1016/j.wasman.2020.08.016.

[7] Eurostat (Statistical Office of the European Communities), Municipal waste statistics. https://ec.europa.eu/eurostat/statistics-explained/index.php?title=Municipal_waste_statistics#Municipal_waste_generation, 2023.

[8] United States Environmental Protection Agency (US EPA), National overview: facts and figures on materials, wastes and recycling. https://www.epa.gov/facts-and-figures-about-materials-waste-and-recycling/national-overview-facts-and-figures-materials, 2022.

[9] National Bureau of Statistics of China (NBS), Urban garbage collection and disposal situation. https://data.stats.gov.cn/easyquery.htm?cn=E0103, 2022.

[10] International Renewable Energy Agency (IRENA), Renewable capacity statistics 2022. https://www.irena.org/-/media/Files/IRENA/Agency/Publication/2022/Apr/IRENA_RE_Capacity_Statistics_2022.pdf?rev=460f190dea15442eba8373d9625341ae, 2022.

[11] B. Chen, P. Perumal, M. Illikainen, G. Ye, A review on the utilization of municipal solid waste incineration (MSWI) bottom ash as a mineral resource for construction materials, J. Build. Eng. (2023) 106386, https://doi.org/10.1016/j.jobe.2023.106386.

[12] B. Chen, P. Perumal, F. Aghabeyk, A. Adediran, M. Illikainen, G. Ye, Advances in using municipal solid waste incineration (MSWI) bottom ash as precursor for alkali-activation materials: a critical review, Resour. Conserv. Recycl. 204 (2024) 107516, https://doi.org/10.1016/j.resconrec.2024.107516.

[13] B.C. McLellan, R.P. Williams, J. Lay, A. Van Riessen, G.D. Corder, Costs and carbon emissions for geopolymer pastes in comparison to ordinary portland cement, J. Clean. Prod. 19 (2011) 1080–1090.

[14] G. Habert, C. Ouellet-Plamondon, Recent update on the environmental impact of geopolymers, RILEM Tech, Lett. 1 (2016) 17–23.
[15] G. Habert, J.B.D. De Lacaillerie, N. Roussel, An environmental evaluation of geopolymer based concrete production: reviewing current research trends, J. Clean. Prod. 19 (2011) 1229–1238.
[16] G. Habert, A method for allocation according to the economic behaviour in the EU-ETS for by-products used in cement industry, Int. J. Life Cycle Assess. 18 (2013) 113–126.
[17] M. Weil, K. Dombrowski, A. Buchwald, Life-cycle analysis of geopolymers, in: Geopolymers, Elsevier, 2009, pp. 194–210.
[18] T.S. Ng, Y.L. Voo, S.J. Foster, Sustainability with ultra-high performance and geopolymer concrete construction, in: Innov. Mater. Tech. Concr. Constr., Springer, 2012, pp. 81–100.
[19] T. Stengel, D. Heinz, J. Reger, Life cycle assessment of geopolymer concrete–what is the environmental benefit, in: Proceeding 24th Bienn, Conf. Concr. Inst. Aust., 2009.
[20] P. den Heede, N. De Belie, Environmental impact and life cycle assessment (LCA) of traditional and 'green'concretes: literature review and theoretical calculations, Cem. Concr. Compos. 34 (2012) 431–442.
[21] A. Heath, K. Paine, M. McManus, Minimising the global warming potential of clay based geopolymers, J. Clean. Prod. 78 (2014) 75–83.
[22] C. Xue, V. Sirivivatnanon, A. Nezhad, Q. Zhao, Comparisons of alkali-activated binder concrete (ABC) with OPC concrete - a review, Cem. Concr. Compos. 135 (2023) 104851, https://doi.org/10.1016/j.cemconcomp.2022.104851.
[23] A. Wang, Y. Zheng, Z. Zhang, K. Liu, Y. Li, L. Shi, D. Sun, The durability of alkali-activated materials in comparison with ordinary portland cements and concretes: a review, Engineering 6 (2020) 695–706, https://doi.org/10.1016/j.eng.2019.08.019.
[24] J.L. Provis, Alkali-activated materials, Cement Concr. Res. 114 (2018) 40–48, https://doi.org/10.1016/j.cemconres.2017.02.009.
[25] J.L. Provis, J.S.J. Van Deventer, Alkali Activated Materials: State-Of-The-Art Report, RILEM TC 224-AAM, Springer Science \& Business Media, 2013.
[26] International Energy Agency (IEA), Cement Technology roadmap: carbon emissions reductions up to 2050. https://www.iea.org/reports/cement-technology-roadmap-carbon-emissions-reductions-up-to-2050, 2009.
[27] B. Chen, Y. Zuo, S. Zhang, L.M. de Lima Junior, X. Liang, Y. Chen, M.B. van Zijl, G. Ye, Reactivity and leaching potential of municipal solid waste incineration (MSWI) bottom ash as supplementary cementitious material and precursor for alkali-activated materials, Constr. Build. Mater. 409 (2023) 133890, https://doi.org/10.1016/j.conbuildmat.2023.133890.
[28] S. Casanova, R.V. Silva, J. de Brito, M.F.C. Pereira, Mortars with alkali-activated municipal solid waste incinerator bottom ash and fine recycled aggregates, J. Clean. Prod. 289 (2021), https://doi.org/10.1016/j.jclepro.2020.125707.
[29] R. Carvalho, R.V. Silva, J. de Brito, M.F.C. Pereira, Alkali activation of bottom ash from municipal solid waste incineration: optimization of NaOH- and Na 2SiO3-based activators, J. Clean. Prod. 291 (2021), https://doi.org/10.1016/j.jclepro.2021.125930.
[30] G. Huang, K. Yang, L. Chen, Z. Lu, Y. Sun, X. Zhang, Y. Feng, Y. Ji, Z. Xu, Use of pretreatment to prevent expansion and foaming in high-performance MSWI bottom ash alkali-activated mortars, Constr. Build. Mater. 245 (2020), https://doi.org/10.1016/j.conbuildmat.2020.118471.
[31] À. Maldonado-Alameda, J. Giro-Paloma, A. Alfocea-Roig, J. Formosa, J. M. Chimenos, Municipal solid waste incineration bottom ash as sole precursor in the alkali-activated binder formulation, Appl. Sci. 10 (2020), https://doi.org/10.3390/APP10124129.
[32] I. Lancellotti, M. Cannio, F. Bollino, M. Catauro, L. Barbieri, C. Leonelli, Geopolymers: an option for the valorization of incinerator bottom ash derived "end of waste,", Ceram. Int. 41 (2015) 2116–2123, https://doi.org/10.1016/j.ceramint.2014.10.008.
[33] G. Huang, Y. Ji, J. Li, L. Zhang, X. Liu, B. Liu, Effect of activated silica on polymerization mechanism and strength development of MSWI bottom ash alkali-activated mortars, Constr. Build. Mater. 201 (2019) 90–99, https://doi.org/10.1016/j.conbuildmat.2018.12.125.
[34] G. Huang, Y. Ji, L. Zhang, J. Li, Z. Hou, The influence of curing methods on the strength of MSWI bottom ash-based alkali-activated mortars: the role of leaching of OH− and free alkali, Constr. Build. Mater. 186 (2018) 978–985, https://doi.org/10.1016/j.conbuildmat.2018.07.224.
[35] G. Huang, L. Yuan, Y. Ji, B. Liu, Z. Xu, Cooperative action and compatibility between Portland cement and MSWI bottom ash alkali-activated double gel system materials, Constr. Build. Mater. 209 (2019) 445–453, https://doi.org/10.1016/j.conbuildmat.2019.03.141.
[36] G. Huang, K. Yang, Y. Sun, Z. Lu, X. Zhang, L. Zuo, Y. Feng, R. Qian, Y. Qi, Y. Ji, Z. Xu, Influence of NaOH content on the alkali conversion mechanism in MSWI bottom ash alkali-activated mortars, Constr. Build. Mater. 248 (2020), https://doi.org/10.1016/j.conbuildmat.2020.118582.
[37] L. Jin, G. Huang, Y. Li, X. Zhang, Y. Ji, Z. Xu, Positive influence of liquid sodium silicate on the setting time, polymerization, and strength development mechanism of mswi bottom ash alkali-activated mortars, Materials 14 (2021), https://doi.org/10.3390/ma14081927.
[38] B. Chen, J. Chen, F.F. de Mendonça Filho, Y. Sun, M.B. van Zijl, O. Copuroglu, G. Ye, Characterization and mechanical removal of metallic aluminum (Al) embedded in weathered municipal solid waste incineration (MSWI) bottom ash for application as supplementary cementitious material, Waste Manag. 176 (2024) 128–139, https://doi.org/10.1016/j.wasman.2024.01.031.
[39] Y. Liu, K.S. Sidhu, Z. Chen, E.H. Yang, Alkali-treated incineration bottom ash as supplementary cementitious materials, Constr. Build. Mater. 179 (2018) 371–378, https://doi.org/10.1016/j.conbuildmat.2018.05.231.
[40] X.C. Qiao, M. Tyrer, C.S. Poon, C.R. Cheeseman, Novel cementitious materials produced from incinerator bottom ash, Resour. Conserv. Recycl. 52 (2008) 496–510, https://doi.org/10.1016/j.resconrec.2007.06.003.
[41] X.C. Qiao, M. Tyrer, C.S. Poon, C.R. Cheeseman, Characterization of alkali-activated thermally treated incinerator bottom ash, Waste Manag. 28 (2008) 1955–1962, https://doi.org/10.1016/j.wasman.2007.09.007.
[42] B. Chen, G. Ye, The role of water-treated municipal solid waste incineration (MSWI) bottom ash in microstructure formation and strength development of blended cement pastes, Cement Concr. Res. 178 (2024) 107440, https://doi.org/10.1016/j.cemconres.2024.107440.
[43] M. Nedeljković, Z. Li, G. Ye, Setting, strength, and autogenous shrinkage of alkali-activated fly ash and slag pastes: effect of slag content, Materials 11 (2018), https://doi.org/10.3390/ma11112121.
[44] B. Sun, Y. Sun, G. Ye, G. De Schutter, A mix design methodology of slag and fly ash-based alkali-activated paste, Cem. Concr. Compos. 126 (2022) 104368, https://doi.org/10.1016/j.cemconcomp.2021.104368.
[45] K. Scrivener, R. Snellings, B. Lothenbach, A Practical Guide to Microstructural Analysis of Cementitious Materials, CRC Press, Boca Raton, FL, USA, 2016.
[46] S. Ma, R. Snellings, X. Li, X. Shen, K.L. Scrivener, Alite-ye'elimite cement: synthesis and mineralogical analysis, Cement Concr. Res. 45 (2013) 15–20, https://doi.org/10.1016/j.cemconres.2012.10.020.
[47] Z. Zhang, Y. Zhu, H. Zhu, Y. Zhang, J.L. Provis, H. Wang, Effect of drying procedures on pore structure and phase evolution of alkali-activated cements, Cem. Concr. Compos. 96 (2019) 194–203, https://doi.org/10.1016/j.cemconcomp.2018.12.003.
[48] NEN-EN 196-1, Methods of Testing Cement - Part 1, Determination of strength, 2016. https://connect.nen.nl/Standard/Detail/219352?compId=10037&collectionId=0.
[49] Standard practice for measuring hydration kinetics of hydraulic cementitious mixtures using isothermal calorimetry. https://www.astm.org/c1679-17.html, 2023.
[50] S. Chen, S. Ruan, Q. Zeng, Y. Liu, M. Zhang, Y. Tian, D. Yan, Pore structure of geopolymer materials and its correlations to engineering properties: a review, Constr. Build. Mater. 328 (2022) 127064, https://doi.org/10.1016/j.conbuildmat.2022.127064.
[51] M. Nedeljković, B. Šavija, Y. Zuo, M. Luković, G. Ye, Effect of natural carbonation on the pore structure and elastic modulus of the alkali-activated fly ash and slag pastes, Constr. Build. Mater. 161 (2018) 687–704, https://doi.org/10.1016/j.conbuildmat.2017.12.005.
[52] E.P. Barrett, L.G. Joyner, P.P. Halenda, The determination of pore volume and area distributions in porous substances. I. Computations from nitrogen isotherms, J. Am. Chem. Soc. 73 (1951) 373–380.
[53] S. Roels, J. Elsen, J. Carmeliet, H. Hens, Characterisation of pore structure by combining mercury porosimetry and micrography, Mater. Struct. 34 (2001) 76–82, https://doi.org/10.1007/BF02481555.
[54] G. Ye, Experimental Study and Numerical Simulation of the Development of the Microstructure and Permeability of Cementitious Materials, 2003.
[55] Y. Ma, Microstructure and Engineering Properties of Alkali Activated Fly Ash-As an Environment Friendly Alternative to Portland Cement, 2013.
[56] J.M.S. Prewitt, M.L. Mendelsohn, The analysis of cell images, Ann. N. Y. Acad. Sci. 128 (1966) 1035–1053, https://doi.org/10.1111/j.1749-6632.1965.tb11715.x.
[57] V. Kocaba, E. Gallucci, K.L. Scrivener, Methods for determination of degree of reaction of slag in blended cement pastes, Cement Concr. Res. 42 (2012) 511–525, https://doi.org/10.1016/j.cemconres.2011.11.010.
[58] I. García Lodeiro, A. Fernández-Jimenez, A. Palomo, D.E. Macphee, Effect on fresh C-S-H gels of the simultaneous addition of alkali and aluminium, Cement Concr. Res. 40 (2010) 27–32, https://doi.org/10.1016/j.cemconres.2009.08.004.
[59] B. Walkley, R. San Nicolas, M.-A. Sani, G.J. Rees, J.V. Hanna, J.S.J. van Deventer, J.L. Provis, Phase evolution of C-(N)-ASH/NASH gel blends investigated via alkali-activation of synthetic calcium aluminosilicate precursors, Cement Concr. Res. 89 (2016) 120–135.
[60] I. Garcia-Lodeiro, A. Palomo, A. Fernández-Jiménez, D.E. Macphee, Compatibility studies between NASH and CASH gels. Study in the ternary diagram Na2O–CaO–Al2O3–SiO2–H2O, Cement Concr. Res. 41 (2011) 923–931.
[61] M.R. Filgueiras, G. La Torre, L.L. Hench, Solution effects on the surface reactions of a bioactive glass, J. Biomed. Mater. Res. 27 (1993) 445–453, https://doi.org/10.1002/jbm.820270405.
[62] M. Torres-Carrasco, A. Palomo, F. Puertas, Sodium silicate solutions from dissolution of glass wastes. Statistical Analysis, 2014.
[63] H. Xu, J.S.J. Van Deventer, The geopolymerisation of alumino-silicate minerals, Int. J. Miner. Process. 59 (2000) 247–266, https://doi.org/10.1016/S0301-7516(99)00074-5.
[64] F.B. Reig, J.V.G. Adelantado, M.C.M. Moya Moreno, FTIR quantitative analysis of calcium carbonate (calcite) and silica (quartz) mixtures using the constant ratio method. Application to geological samples, Talanta 58 (2002) 811–821, https://doi.org/10.1016/S0039-9140(02)00372-7.
[65] C.K. Huang, P.F. Kerr, Infrared study of the carbonate minerals, Am. Mineral. 45 (1960) 311–324.
[66] A. Fernández-Jiménez, A. Palomo, Mid-infrared spectroscopic studies of alkali-activated fly ash structure, Microporous Mesoporous Mater. 86 (2005) 207–214.
[67] J.R. Sweet, W.B. White, Study of sodium silicate glasses and liquids by infrared reflectance spectroscopy, Phys. Chem. Glasses 10 (1969) 246.

[68] A. Maldonado-Alameda, J. Giro-Paloma, J. Mañosa, J. Formosa, J.M. Chimenos, Alkali-activated binders based on the coarse fraction of municipal solid waste incineration bottom ash. Boletín La Soc. Española Cerámica Y Vidr, 2021, https://doi.org/10.1016/j.bsecv.2020.12.002.
[69] Y. Wang, Y. Cao, Z. Zhang, J. Huang, P. Zhang, Y. Ma, H. Wang, Study of acidic degradation of alkali-activated materials using synthetic C-(N)-A-S-H and N-A-S-H gels, Compos. Part B Eng. 230 (2022) 109510, https://doi.org/10.1016/j.compositesb.2021.109510.
[70] S. Chithiraputhiran, N. Neithalath, Isothermal reaction kinetics and temperature dependence of alkali activation of slag, fly ash and their blends, Constr. Build. Mater. 45 (2013) 233–242.
[71] J.L. Provis, J.S.J. Van Deventer, Geopolymerisation kinetics. 2. Reaction kinetic modelling, Chem. Eng. Sci. 62 (2007) 2318–2329.
[72] P. Lawrence, M. Cyr, E. Ringot, Mineral admixtures in mortars: effect of inert materials on short-term hydration, Cement Concr. Res. 33 (2003) 1939–1947, https://doi.org/10.1016/S0008-8846(03)00183-2.
[73] B. Lothenbach, K. Scrivener, R.D. Hooton, Supplementary cementitious materials, Cement Concr. Res. 41 (2011) 1244–1256, https://doi.org/10.1016/j.cemconres.2010.12.001.
[74] S.A. Bernal, R. San Nicolas, R.J. Myers, R. Mejía de Gutiérrez, F. Puertas, J.S.J. van Deventer, J.L. Provis, MgO content of slag controls phase evolution and structural changes induced by accelerated carbonation in alkali-activated binders, Cement Concr. Res. 57 (2014) 33–43, https://doi.org/10.1016/j.cemconres.2013.12.003.
[75] S. Puligilla, X. Chen, P. Mondal, Does synthesized CSH seed promote nucleation in alkali activated fly ash-slag geopolymer binder? Mater. Struct. 52 (2019) 1–13.
[76] M. Ben Haha, B. Lothenbach, G. Le Saout, F. Winnefeld, Influence of slag chemistry on the hydration of alkali-activated blast-furnace slag — Part I: effect of MgO, Cement Concr. Res. 41 (2011) 955–963, https://doi.org/10.1016/j.cemconres.2011.05.002.
[77] R.J. Myers, S.A. Bernal, J.L. Provis, A thermodynamic model for C-(N-)A-S-H gel: CNASH_ss. Derivation and validation, Cement Concr. Res. 66 (2014) 27–47, https://doi.org/10.1016/j.cemconres.2014.07.005.
[78] R.J. Myers, B. Lothenbach, S.A. Bernal, J.L. Provis, Thermodynamic modelling of alkali-activated slag cements, Appl. Geochem. 61 (2015) 233–247, https://doi.org/10.1016/j.apgeochem.2015.06.006.
[79] V. Stubičan, R. Roy, Infrared spectra of layer-structure silicates, J. Am. Ceram. Soc. 44 (1961) 625–627, https://doi.org/10.1111/j.1151-2916.1961.tb11670.x.
[80] A. Fernández-Jiménez, F. Puertas, Effect of activator mix on the hydration and strength behaviour of alkali-activated slag cements, Adv. Cement Res. 15 (2003) 129–136, https://doi.org/10.1680/adcr.2003.15.3.129.
[81] P. Yu, R.J. Kirkpatrick, B. Poe, P.F. McMillan, X. Cong, Structure of calcium silicate hydrate (C-S-H): near-, Mid-, and Far-infrared spectroscopy, J. Am. Ceram. Soc. 82 (1999) 742–748.
[82] M. Sitarz, M. Handke, W. Mozgawa, Identification of silicooxygen rings in SiO2 based on IR spectra, Spectrochim. Acta Part A Mol. Biomol. Spectrosc. 56 (2000) 1819–1823.
[83] M. Sitarz, M. Handke, W. Mozgawa, E. Galuskin, I. Galuskina, The non-ring cations influence on silicooxygen ring vibrations, J. Mol. Struct. 555 (2000) 357–362, https://doi.org/10.1016/S0022-2860(00)00621-9.
[84] J.E. Rossen, K.L. Scrivener, Optimization of SEM-EDS to determine the C–A–S–H composition in matured cement paste samples, Mater. Char. 123 (2017) 294–306.
[85] I. García-Lodeiro, A. Fernández-Jiménez, A. Palomo, D.E. Macphee, Effect of calcium additions on N–A–S–H cementitious gels, J. Am. Ceram. Soc. 93 (2010) 1934–1940.
[86] L. Zheng, W. Wang, Y. Shi, The effects of alkaline dosage and Si/Al ratio on the immobilization of heavy metals in municipal solid waste incineration fly ash-based geopolymer, Chemosphere 79 (2010) 665–671, https://doi.org/10.1016/j.chemosphere.2010.02.018.
[87] M. Ben Haha, B. Lothenbach, G. Le Saout, F. Winnefeld, Influence of slag chemistry on the hydration of alkali-activated blast-furnace slag — Part II: effect of Al2O3, Cement Concr. Res. 42 (2012) 74–83, https://doi.org/10.1016/j.cemconres.2011.08.005.
[88] F. Chayes, Petrographic Modal Analysis : an Elementary Statistical Appraisal, Wiley, New York, 1956.